Luminescent Iridium(III) Complexes Supported by a Tetradentate Trianionic Ligand Scaffold with Mixed O, N, and C Donor Atoms: Synthesis, Structures, Photophysical Properties, and Material Applications

Daqing Chen,[†,§] Kai Li,[†,§] Xiangguo Guan,[†] Gang Cheng,[†] Chen Yang,[†] and Chi-Ming Che*,[†,‡]

[†]State Key Laboratory of Synthetic Chemistry, Institute of Molecular Functional Materials, HKU-CAS Joint Laboratory on New Materials, and Department of Chemistry, The University of Hong Kong, Pokfulam Road, Hong Kong, People's Republic of China
[‡]HKU Shenzhen Institute of Research and Innovation, Shenzhen 518053, People's Republic of China

ⓢ *Supporting Information*

ABSTRACT: A panel of tetradentate H_3-O^N^C^O ligands has been synthesized and employed as a trianionic scaffold for preparing $[Ir^{III}(O^\wedge N^\wedge C^\wedge O)(L)_2]$, with L = a wide variety of neutral ligands, and also $[Ir^{III}(O^\wedge N^\wedge C^\wedge O)(C\equiv NAr)(NH_2Ar)]$, $[Ir^{III}(O^\wedge N^\wedge C^\wedge O)(C\equiv NAr)(X)]$ (Ar = 2,6-$Me_2C_6H_3$; X = 1-methylimidazole, PPh_3, pyridine), and $[Ir^{III}(O^\wedge N^\wedge C^\wedge O)-(NHC)]_2$ (NHC = N-heterocyclic carbene). X-ray crystal structure analysis and photophysical studies (including variable-temperature emission lifetime measurements and nanosecond time-resolved emission and absorption spectroscopy) were performed. $[Ir(O^\wedge N^\wedge C^\wedge O)(L)_2]$ display a moderately strong phosphorescence at room temperature (emission quantum yields up to 18% in solution, 51% in PMMA film), with the luminescent properties being strongly affected by axial L ligands. The use of $[Ir(O^\wedge N^\wedge C^\wedge O)(NHC)_2]$ as a phosphorescent emitter in a solution-processed organic light-emitting diode device generated a red electrophosphorescence with an EQE of 10.5% and CIE chromaticity coordinates of (0.64, 0.36).

L = MeIm, pyridine, pyridazine, PPh_3, NHC

L' = Aniline, MeIm, pyridine, PPh_3
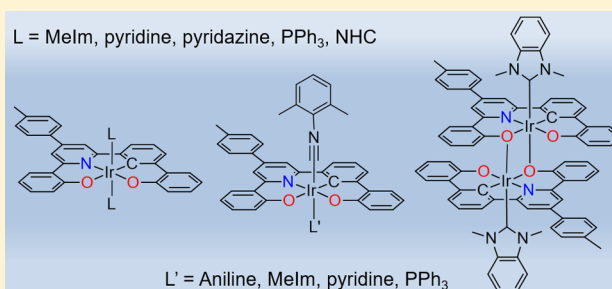
■ INTRODUCTION

The design of new ligands is pivotal in the advancement of transition-metal chemistry. Over the past decades, there have been numerous reports on multianionic ligands for their capability to stabilize metal ions in high oxidation states and their chelating effects imparting thermal and chemical stability to the resulting metal complexes. Porphyrin and Schiff base type ligands are the most commonly studied planar tetradentate ligand scaffolds, with their transition-metal complexes shown to have profound applications in diverse areas such as catalysis,[1,2] materials science,[3,4] and medicines.[5] Iridium(III) complexes supported by porphyrins or salen ligands have shown remarkable catalytic activities in various organic transformations, including cyclopropanation, C−H insertion, and Si−H insertion.[6] In 2011, Koren and co-workers reported a series of cationic porphyrin-based red to NIR (near-infrared) emitting Ir(III) complexes with emission efficiencies of up to ca. 30%.[7] The porphyrin and salen ligands are dianionic and, upon coordination to trivalent metal ions, such as iridium(III) and gold(III), usually afford cationically charged metal complexes. We have been interested in developing tetradentate trianionic (TDTA) ligands that are suitable for the synthesis of charge-neutral complexes of trivalent metal ions and for the stabilization of high-valent metal−ligand bonded complexes.[8] Examples of planar TDTA ligands in the literature mainly

comprise corroles[9] and bis(phenolate)dipyrrins,[10] which belong to the N^N^N^N and O^N^N^O donor systems, respectively.

As depicted in Chart 1, bidentate and tridentate ligands are commonly used to prepare neutral luminescent Ir(III) complexes.[11] In contrast, photophysical and photochemical investigations of neutral Ir(III) complexes containing planar tetradentate ligands are relatively sparse.[12−14] Gray, Gross, and co-workers first developed a class of neutral Ir(III)-corrole complexes[12] (I in Chart 1), which display NIR phosphorescence arising from corrole ligand-centered transitions.[12c] However, the emission quantum yields of Ir(III)-corrole complexes,[12c,13,14] and also iridium monoazaporphyrin derivatives,[13a] are very low (≤3.09%) in degassed solutions. It is noted that these aforementioned tetradentate ligands do not contain strongly σ donating C atoms which could be useful for achieving both high emission quantum yields and robustness of the metal complexes. Furuta and co-workers recently developed a class of neutral Ir(III) complexes supported by a novel type of trianionic benzonorrole ligand containing one C-donor atom (J in Chart 1).[14] In comparison to the Ir(III)-corrole analogue, these organoiridium(III) complexes exhibit significantly red shifted emission (λ >900 nm, quantum yield ≤0.62%). Lash

Chart 1. Structures of a Selection of the Reported Ir(III) Complexes with Different Combinations of Coordination Ligands
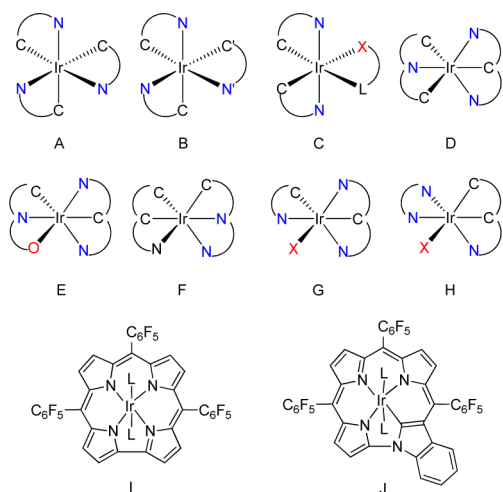
and co-workers reported an Ir(III) complex of trianionic carbaporphyrin (which also contains one C-donor atom).[15] The luminescence properties of this complex have not been reported. Yam and co-workers recently reported a class of strongly luminescent tetradenatate cyclometalated alkynylgold-(III) complexes generated through a postsynthetic ligand modification.[16]

Herein we report the design, synthesis, structure, and spectroscopic characteristics of a new class of charge-neutral [Ir-(O^N^C^O)(L)$_2$] and [Ir(O^N^C^O)(L)(L′)] complexes supported by planar O^N^C^O TDTA ligand scaffolds. These complexes exhibit moderate emission quantum yields of up to 18% in degassed CH$_2$Cl$_2$ and 51% in PMMA thin film at room temperature. The axial ligands (L or L′) have been observed to have profound effects on the emission properties of the Ir(III) complexes. One example of these [Ir-(O^N^C^O)(L)$_2$] complexes has been used to fabricate red OLEDs with satisfactory performance.

■ **RESULTS AND DISCUSSION**

Synthesis of Ligands H$_3$L1−H$_3$L3. We have recently developed a series of tetradentate dianionic O^N^C^N ligands for the preparation of strongly emissive Pt(II)[17] and Pd(II)[18] complexes. In the current study, we designed a series of TDTA ligands, H$_3$-O^N^C^O (H$_3$L1−H$_3$L3), by replacing the pyridyl ring of H$_2$-O^N^C^N with a phenol moiety (Scheme 1). The

newly designed ligands have extended π conjugation and adopt a tetradentate coordination mode in a planar coordination geometry upon coordination to a metal ion. As depicted in Scheme 1, H$_3$L1 was prepared by two consecutive Pd-(PPh$_3$)$_2$Cl$_2$/K$_2$CO$_3$-mediated Suzuki coupling reactions between arylboronic acid and aryl bromides in a total yield of 28%. This relatively low yield may be attributed to side reactions in the synthesis of 2-bromo-6-(3-bromophenyl)-pyridine, during which a considerable amount of the byproduct 2,6-bis(3-bromophenyl)pyridine was isolated. The synthesis of H$_3$L2 and H$_3$L3 was performed by applying the Krohnke pyridine synthesis method as a key step. 2′-Hydroxyl-4-methylchalcone and 1-[2-(3-bromophenyl)-2-oxoethyl]-pyridinium iodide underwent Michael addition to give 1,5-diketones, which reacted with ammonium acetate in methanol (Scheme 1). Subsequent oxidation gave 2-[6-(3-bromophenyl)-4-p-tolylpyridin-2-yl]phenol. Further Suzuki coupling of the resulting bromides with arylboronic acids afforded H$_3$L2 and H$_3$L3 in much higher total yields of 85% and 87%, respectively.

**Synthesis and Characterization of [Ir(O^N^C^O)(L)$_2$] (1−14).** The synthetic method for Ir(III)-corrole complexes was adopted for the synthesis of complexes [Ir(O^N^C^O)-(L)$_2$] (1−14) (Scheme 2). We conceived that a [(O^N^C^O)-Ir^I(Cod)] intermediate was initially formed by the reaction of the H$_3$-O^N^C^O ligands with [Ir(Cod)Cl]$_2$ and K$_2$CO$_3$ in degassed THF under N$_2$, which was subsequently oxidized to give O^N^C^O-ligated Ir(III) complexes upon exposure to ambient atmosphere. Complexes 1−14 were obtained in moderate to high yields (29−91%) and, except for 2, 8, and 14, are stable both in the solid state and in solution under ambient conditions. The bis-NHC Ir(III) complexes 8 and 14 are not stable upon prolonged standing in solution. During the synthesis of 8 and 14, a minor amount of dinuclear [Ir(O^N^C^O)(NHC)]$_2$ (15 and 16) (Scheme 3) was obtained. Attempts to obtain diffraction-quality crystals of the bis-NHC complexes 8 and 14 by slow evaporation of the corresponding CH$_2$Cl$_2$ solutions (7 days) resulted in the formation of 15 and 16 with structures resembling that of dinuclear (salen)Ru carbene complexes, which have a distorted-octahedral geometry.[19]

Synthesis and Characterization of [Ir(O^N^C^O)(L)(L′)]. In attempts to prepare Ir(III)-L2 complexes containing axial isocyanide (C≡NAr) ligands, [Ir(O^N^C^O)(C≡NAr)-(NH$_2$Ar)] (17 and 18) were unexpectedly obtained as the major products (Scheme 4), both of which contain an isocyanide and an aniline axial ligand. The aniline ligand is conceived to come from hydrolysis of the isocyanide ligand.
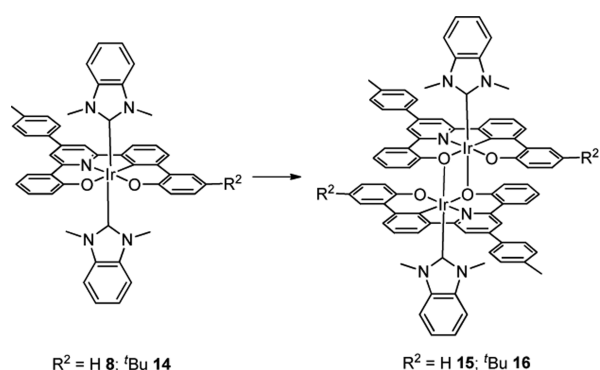
Scheme 1. Synthesis of Tetradentate Ligands H$_3$L1−H$_3$L3
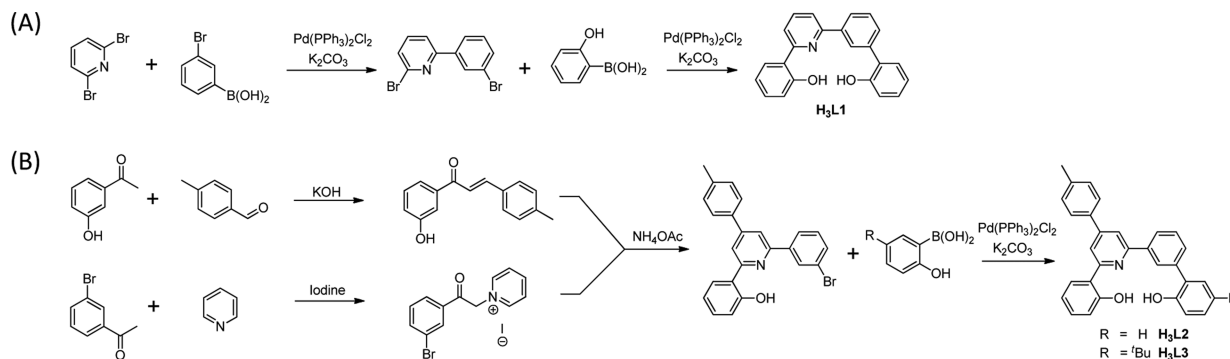
Scheme 2. Synthesis and Structures of Complexes 1−14

$R^2 = H$ **3**   **4**   **5**   **6**   **7**   **8**

$R^2 = {}^tBu$ **9**   **10**   **11**   **12**   **13**   **14**
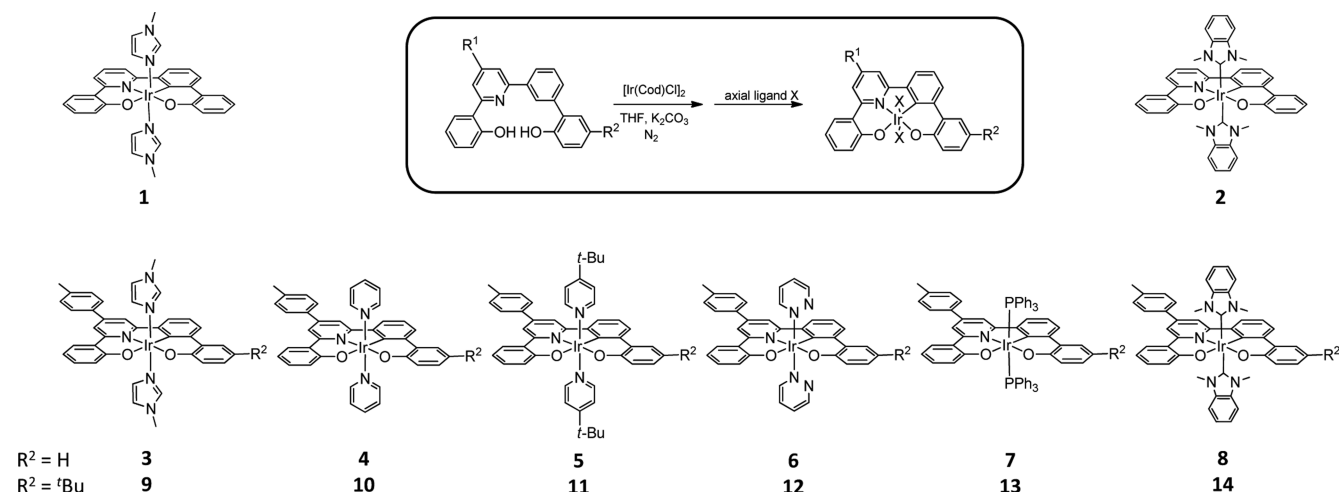
Scheme 3. Synthesis and Structures of Complexes 15 and 16

$R^2 = H$ **8**; ${}^tBu$ **14** $R^2 = H$ **15**; ${}^tBu$ **16**

Scheme 4. Synthesis and Structures of Complexes 17−21
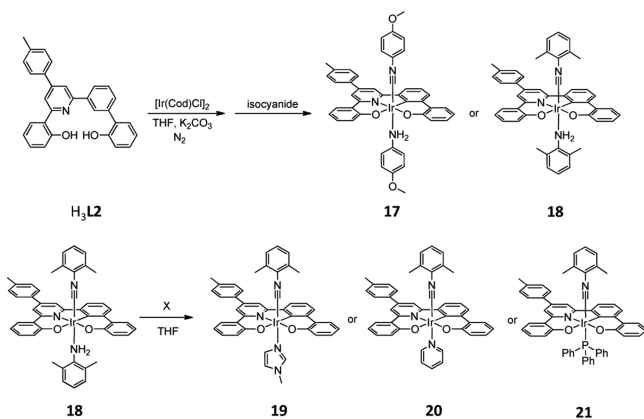
Stynes and co-workers[20] reported that the isocyanide ligand of [Fe(Pc)(C≡NR)$_2$] (Pc = phthalocyanine) undergoes ligand dissociation as a result of the strong trans effect of the isocyanide ligand in solution. According to their findings, the dissociation rate of isocyanide increases by 10^4-fold by changing the trans axial amine ligand to an isocyanide ligand. The ^{1}H NMR signal of a primary amine coordinated to a metal ion usually appears as a singlet. However, the signals for the two N−H protons in **17** appear as two doublets at 5.32 and 4.57 ppm. The split of the N−H signals is attributable to a restricted rotation of the Ir−N(aniline) bond caused by a push−pull interaction involving hyperconjugation of an NH σ orbital

(push) and a π^* orbital of the isocyanide CN moiety (pull). Reactions of **18** with PPh$_3$, pyridine, and 1-methylimidazole (X) generated [Ir(O∧N∧C∧O)(C≡NAr)(X)] (**19−21**) in good yields (77−89%). All complexes were characterized by various methods, including ^{1}H NMR, FAB-MS, and elemental analysis.

Variable-Temperature ^{1}H NMR of Complexes 8 and 19. It is worth noting that although the [Ir(O∧N∧C∧O)] motif is ruffled, as revealed by the crystal structure of **9** (vide infra), the ^{1}H NMR spectra of **1**, **3**, and **9** show singlet peaks attributed to the N−CH_3 groups on the axial 1-methylimidazole (MeIm) ligands, revealing the fluxional behavior of the O∧N∧C∧O ligand and fast rotation of the axial ligands around the Ir−N(MeIm) bonds in solution. Instead, the ^{1}H NMR spectra of **8** and **14** show broad singlet peaks at around 3.52 ppm, assigned to the methyl groups on the NHC ligands; the peak broadening effect is suggestive of a moderate rotation rate of the axial NHC ligands on the NMR time scale, possibly due to the close proximity of the N−CH_3 groups to the distorted Ir-O∧N∧C∧O plane. We thus examined the temperature effect on the ^{1}H NMR spectrum of **8**. As shown in Figure 1, when the temperature was lowered, the N−CH_3 signal at 3.56 ppm for **8** first becomes a broader peak. Further lowering of the
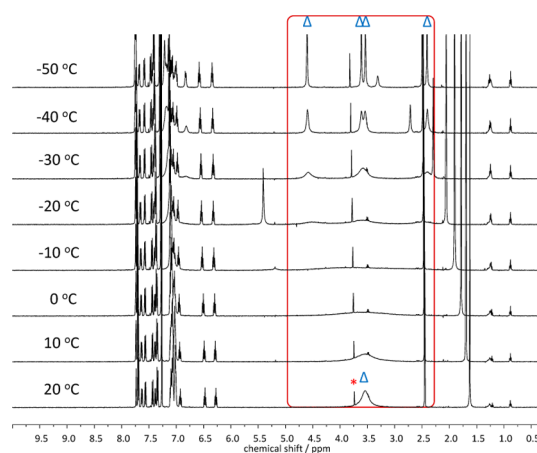

Figure 1. Variable-temperature ^{1}H NMR spectra of **8** in CDCl$_3$. The asterisk denotes the residual solvent peak, and △ denotes the split signals of the N−CH_3 protons.

temperature induces four discernible peaks at 4.60, 3.61, 3.54, and 2.41 ppm, revealing a slower rotation of the NHC ligands. On the other hand, in the examined temperature range, the chemical shifts for aromatic protons only show minor changes, suggesting that O^N^C^O is minimally affected by temperature changes. The ^{1}H NMR spectra of **19** at a wide range of temperatures (220−363 K) were also found to show similar changes (Figure S1 in the Supporting Information).

Thermal Stability. Thermogravimetric analysis (TGA) and differential scanning calorimetry (DSC) experiments of **4** and **8** were performed under N_2 (Figure S2 in the Supporting Information). Complex **4** started to decompose at ca. 275 °C; the weight loss of ca. 20% reached a plateau at 302 °C. This decomposition is attributable to the loss of two axial pyridine ligands (calculated weight loss of 20.3%). The second and third stages of decomposition started at 330 and 468 °C, respectively. The second weight loss is likely due to the loss of the tolyl moiety at the peripheral position. The last decomposition stage with T_d > 468 °C is assigned to decomposition of the O^N^C^O ligand framework. Complex **8** shows a decomposition profile different from that of **4**, with decomposition starting at 320 °C, followed by continuous weight loss at temperatures higher than 440 °C. A glass transition was not observed prior to the decomposition for each complex.

X-ray Crystal Structures. Crystals of **4**, **9**, **13**, **16**, **17**, and **19−21** suitable for X-ray diffraction analysis were obtained by slow diffusion of hexane into the respective chloroform solutions or by slow evaporation of a mixed dichloromethane/hexane solution of the corresponding complexes. The crystallographic data and selected bond distances and angles are compiled in Tables S1 and S2 in the Supporting Information, respectively. All of the complexes adopt a distorted-octahedral geometry with the O^N^C^O ligand scaffold in the equatorial plane. To facilitate comparison, complexes **4**, **9** and **13**, with the aromatic rings labeled P1−P5, are presented in Figure 2. Taking **4** as an example, within the O^N^C^O ligand scaffold, the twists among the P2, P3, and P4 rings are minor, with P2^P3 and P3^P4 torsion angles of 6.46 and 3.82°, respectively. The twist between P1 and P2 is relatively more distinct, with a torsion angle between the two
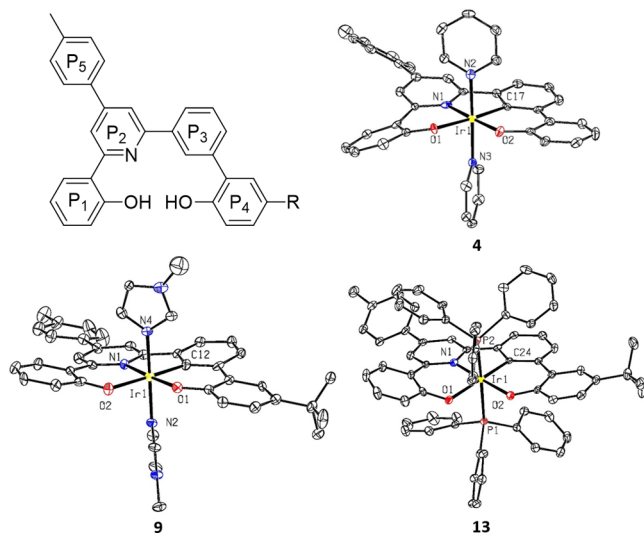
planes of 23.45°. The iridium atom resides essentially on the plane defined by the four coordinating O, N, C, and O atoms with a very small deviation from the plane of 0.02 Å. The Ir(1)−O(1) distance of 2.092(4) Å is slightly longer than that of Ir(1)−O(2) (2.030(3) Å), due to the trans effect of the deprotonated C-donor atom. The chelate angles around the iridium atom within the O^N^C^O plane are 83.3−94.30°. The Ir−N(ax-py) distances of 2.041(4) and 2.047(4) Å are similar to those found in [Ir(corrole)(Py)$_2$] (2.05−2.06 Å).[12c] The two axial pyridine ligands bind to the Ir(III) ion with their planes perpendicular to the Ir−O^N^C^O plane, while they are mutually almost orthogonal with a torsion angle of 88.40°, which is in stark contrast to the case for the [Ir(corrole)(Py)$_2$] complex, in which the two pyridine planes are aligned almost in parallel.[12c] The twisting angles of P1 with respect to P2 in **9** and **13** are 13.24 and 20.93°, respectively. The Ir−P distances of 2.3614(7) and 2.3543(7) Å in **13** are comparable to those of the reported Ir(III) complexes containing axial triphenylphosphine ligands.[21] Notably, the torsion angle of 12.22° between P2 and P5 in **9** is much smaller than those in **4** (38.18°) and **13** (29.64°). As shown in Figure S3 in the Supporting Information, the molecules in the crystal structure of **9** are arranged in pairs and, within each pair, the two molecules interact with each other with the P1, P2, and P5 rings in a head-to-tail manner. This intermolecular interaction, with a π−π distance of around 3.6 Å, probably forces the P5 ring to adopt a relatively coplanar configuration with respect to the P2 ring.

Complex **16** has a μ-O-bridged structure with an inversion center between the two Ir-O^N^C^O-NHC units (Figure 3).
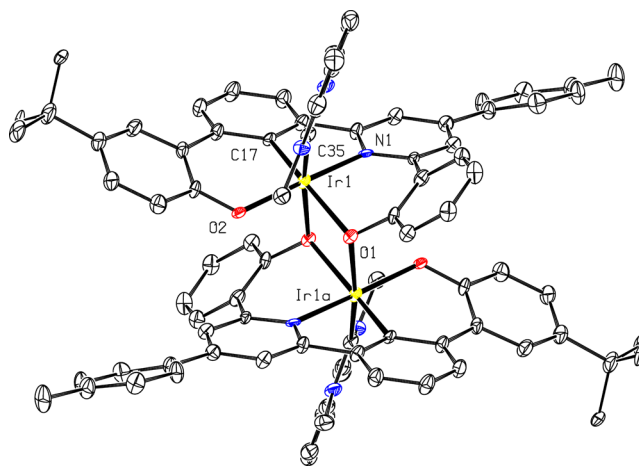
Figure 3. ORTEP plot (50% probability ellipsoids) of **16** with hydrogen atoms omitted for clarity.

The Ir(III)···Ir(III) distance in **16** is 3.336 Å, indicating the absence of a metallophilic interaction. The two Ir(III)-**L3**-NHC fragments are arranged in a slipped manner in which an Ir(III) center is coordinated by an O atom of the other half motif. The Ir(1)−O(1′) distance of 2.136(5) Å is shorter than that of Ir(1)−O(1) at 2.180(4) Å. The Ir−C(NHC) distance of 1.962(7) Å is shorter than those of other reported Ir(III)-NHC complexes (1.989−2.137 Å).[22] The plane of the NHC ligand bisects the N(1)−Ir(1)−C(17) angle, likely to avoid close contact of the methyl groups of the NHC ligand with P1 and P4.

Complex **17** crystallized in a triclinic space group. In each unit cell there are four molecules falling into two pairs (see

Figure 2. ORTEP plots (50% probability ellipsoids) of **4**, **9**, and **13** with hydrogen atoms omitted for clarity.

Figure S4 in the Supporting Information). As depicted in Figure 4, a notable feature of **17** is the remarkably distorted

17

19

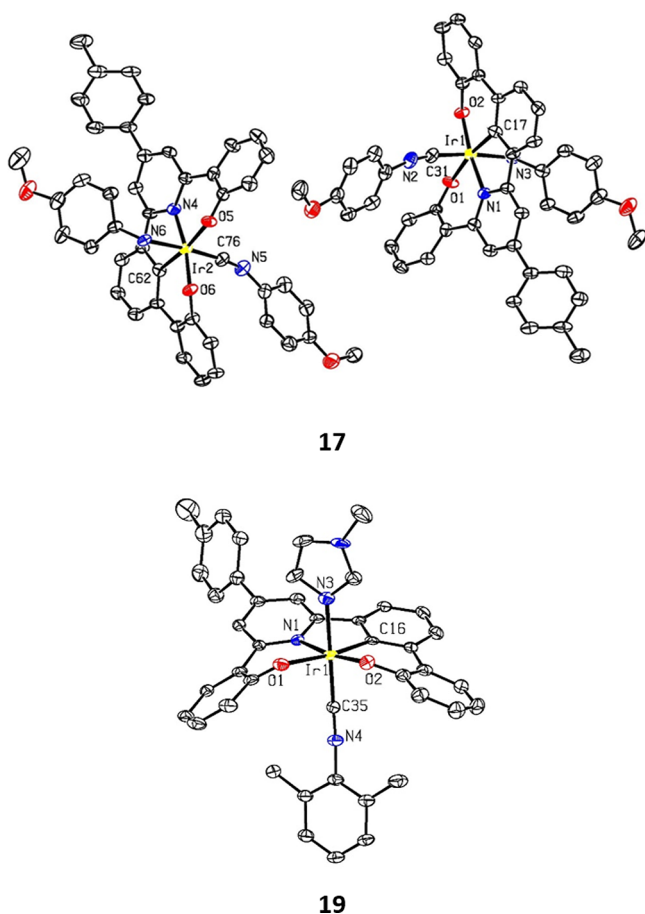**Figure 4.** ORTEP plots (50% probability ellipsoids) of **17** and **19** with hydrogen atoms omitted for clarity.

saddlelike O^N^C^O skeleton arching toward the isocyanide ligand. Within each pair, the mutual orientations of the OMe groups on the isocyanide and the aniline ligands are different for the two molecules. However, the structural parameters of the two isomers, including the two Ir−N(aniline) distances (2.170(5) and 2.171(6) Å) and C≡N (isocyanide) distances (around 1.16 Å) are close to each other.[21] The structure of **19** is also shown in Figure 4, and those of **20** and **21** are shown in Figure S5 in the Supporting Information. All three complexes have saddle-shaped O^N^C^O ligands with the P1 and P4 rings bent toward the isocyanide ligand, as in **17**. The slightly longer Ir−N$_{MeIm}$, Ir−N$_{Py}$, and Ir−P(PPh$_3$) distances of 2.081(4), 2.111(3), and 2.383(3) Å in **19−21** are comparable to those in the corresponding complexes **9**, **4**, and **13** (average distance of two axial Ir−L bonds: 2.041, 2.044, 2.358 Å), respectively, which is ascribed to the strong trans effect of isocyanide ligands. The larger distortion in **20** is evidenced by the 0.112 Å displacement of the iridium atom from the O^N^C^O plane, while for **21** the displacement is 0.06 Å and the four chelate angles within the [Ir(O^N^C^O)] core amount to 360°.

Electrochemistry. The electrochemical properties of **3−8** were examined by cyclic voltammetry in CH$_2$Cl$_2$ (0.1 M [^{n}Bu$_4$N]PF$_6$ as the supporting electrolyte). All of these complexes show multiple irreversible oxidation waves and no reduction waves at potentials down to −2.5 V vs Cp$_2$Fe$^{+/0}$. In

the case of **8**, three oxidation peaks (E_{pa}) appear at 0.10, 0.70, and 1.10 V vs Cp$_2$Fe$^{+/0}$ (Figure 5). When the oxidative scan
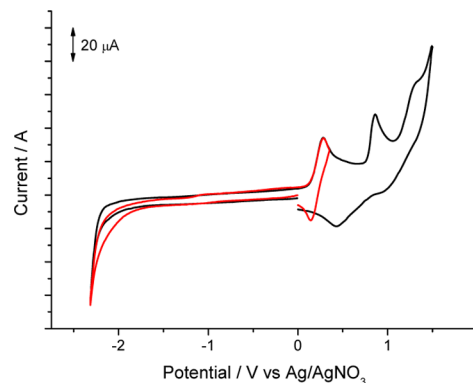

Figure 5. Cyclic voltammograms of **8** (1 mM) in CH$_2$Cl$_2$ with ^{n}Bu$_4$NPF$_6$ (0.1 M) as the supporting electrolyte (for Cp$_2$Fe$^{+/0}$, $E_{1/2}$ = 0.15 V).

was reversed immediately after the appearance of the first oxidation peak, a cathodic wave was observed, revealing the quasi-reversible nature of this oxidation process ($E_{1/2}$ = 0.05 V vs Cp$_2$Fe$^{+/0}$). A similar behavior was observed for the other complexes **3−7** (Figure S6), with E_{pa} for the first oxidation couples at 0.05−0.23 V vs Cp$_2$Fe$^{+/0}$. The dependence of the first E_{pa} value on the electronic properties of the axial ligands supports the involvement of Ir d orbitals in the HOMOs. The less σ donating and more strongly π accepting property of pyridine, 4-*tert*-butylpyridine, and pyridazine cause the first oxidation peaks for **4−6** to occur at a more positive potential, due to their stabilized dπ orbitals. DFT calculations (*vide infra*) reveal that HOMOs of **3**, **4**, and **8** are mainly localized on Ir d orbitals and π(P4) orbitals of the O^N^C^O ligand.

Absorption Spectra. The complexes are classified into four groups to elucidate the effects of the O^N^C^O ligand and axial ligands on the photophysical properties of the Ir(III) complexes; :(1) complexes **3−8** supported by ligand **L2** and with different axial ligands, (2) complexes **1**, **3**, and **9** bearing the same axial MeIm ligands with different O^N^C^O ligands, (3) complexes **2**, **8**, and **14** bearing the same axial NHC ligand with different O^N^C^O ligands and **15** as the dimeric derivative of **14**, and (4) heteroleptic complexes **19−21** bearing ligand **L2**. The photophysical data are summarized in Table 1. The absorption spectrum of **3** in CH$_2$Cl$_2$ is shown in Figure 6, and the absorption spectra of each group of complexes are shown in Figure S7 in the Supporting Information. In general, all of the complexes exhibit two intense absorption bands at λ <300 nm and ∼330−380 nm. The molar absorptivities for these two bands at their peak wavelengths are in the range of (1.34−6.60) × 10^4 M$^{−1}$ cm$^{−1}$. The absorption of ligand **H$_3$L2** in CH$_2$Cl$_2$ is included in Figure 6 for comparison. On the basis of the good spectral overlap between the absorption bands of **H$_3$L2** and **3** at wavelengths shorter than 300 nm, the strong band at λ <300 nm is assigned to the O^N^C^O ligand-centered (LC) ^{1}π−π* transition. The band at 366 nm for **3** is also assigned mainly to a LC ^{1}π−π* transition probably mixed with intraligand charge-transfer (^{1}ILCT) character; the red shift from that of the free ligand (λ$_{max}$ 323 nm) is due to deprotonation of the ligand upon coordination.

In comparison to the free ligand, **3** shows an additional absorption shoulder at around 400 nm ($\varepsilon \approx 1 \times 10^4$ M$^{−1}$ cm$^{−1}$)

Table 1. Photophysical Data of the Ir(III) Complexes

		emission λ_{max} (nm) (τ (μs)); ϕ (%)				
complex	absorption[a] λ_{max} (nm) (ε (10^{-3} M^{-1} cm^{-1}))	solution[a] (298 K)	solid (298 K)	solid (77 K)	glass (77 K)[b]	PMMA (298 K)[c]
1	283 (16.1), 311 (10.8), 354 (13.4), 393 (6.42), 429 (3.07), 500 (br, 1.42)	597 (1.6); 18	596 (0.1)	588 (0.4)	543 (5.9)	578 (1.4); 16
2	283 (24.2), 295 (sh, 21.6), 339 (br, 14.7), 390 (sh, 6.41), 480 (br, 1.15)	586 (0.5); 12	599 (0.2)	592 (1.2)	531 (5.6), 569	572 (2.5); 41
3	261 (40.8), 283 (29.7), 366 (20.3), 394 (sh, 9.98), 438 (3.33), 500 (br, 1.15)	626 (0.9); 11	d	607 (0.3)	577 (4.5)	601 (1.4); 34
4	263 (44.5), 281 (sh, 36.6), 357 (24.5), 395 (sh, 12.8), 500 (br, 1.06)	611 (0.3); 4	d	572 (0.6)	552 (3.50)	591 (0.6); 4
5	265 (43.2), 279 (38.3), 359 (24.0), 400 (12.3), 500 (br, 1.17)	603 (0.4); 6	609 (0.1)	603 (0.1)	563 (4.4)	588 (0.5); 6
6	349 (21.8), 384 (sh, 10.4), 504 (br, 4.2)	622 (−); 0.15	d	d	577 (40.5)	601 (0.5); 1
7	303 (sh, 21.8), 338 (sh, 16.0), 364 (18.0), 410 (sh, 7.73), 490 (br, 1.00)	573 (−); < 0.1%	574 (0.28)	572 (3.26)	561 (5.2)	584 (1.7); 6
8	260 (43.6), 284 (38.8), 356 (br, 18.1), 392 (sh, 10.7), 480 (br, 1.54)	613 (0.4); 12	625 (0.14)	621 (0.77)	559 (4.1)	596 (1.7); 51
9	266 (45.1), 286 (30.4), 368 (22.8), 404 (9.74), 436 (4.55), 504 (br, 1.77)	631 (1.0); 10	581 (0.1)	569 (1.5)	573 (4.6)	608 (1.5); 38
14	266 (sh, 42.7), 280 (sh, 36.9), 307 (sh, 18.8), 362 (23.3), 396 (sh, 13.8), 480 (br, 1.47)	626 (0.4); 6	634 (0.34)	628 (1.2)	570 (4.03)	601 (1.8); 48
15	279 (66.0), 330 (sh, 38.7), 358 (34.7), 383 (sh, 26.7), 411 (sh, 13.2), 480 (br, 2.33)	581 (0.1); 6	571 (0.15)	571 (1.9)	557 (3.58), 600	565 (1.2) 19
19	260 (58.9), 294 (sh, 34.7), 348 (br, 25.1), 415 (sh, br, 6.26)	564 (0.3); 4	556 (0.21)	537 (3.6)	498 (5.95)	545 (1.6); 21
20	259 (46.0), 291 (sh, 30.5), 346 (18.9), 421 (sh, br, 3.83)	563 (0.06); 1	558 (0.32)	556 (2.5)	517 (5.09)	544 (1.2); 11
21	262 (sh, 59.2), 295 (sh, 32.2), 329 (19.4), 350 (19.2), 427 (sh, br, 4.78)	564 (−); <0.1	d	554 (28.7)	515 (26.6)	554 (0.2); 1

[a]Determined in degassed CH$_2$Cl$_2$ ($\sim$4 × 10^{-5} M). Abbreviations: sh, shoulder; br, broad. The solution emission quantum yields were estimated using [Ru(bpy)$_3$](PF$_6$)$_2$ in degassed CH$_3$CN as a standard (ϕ_r = 0.062). [b]Determined in 2-methyltetrahydrofuran at 77 K. [c]Doped at 5 wt % into PMMA film. [d]Not determined due to very weak emission.
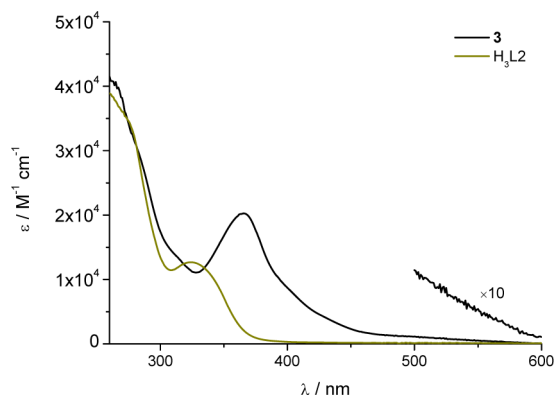

Figure 6. Absorption spectra of **H$_3$L2** and **3** in CH$_2$Cl$_2$ (4 × 10^{-5} M).

and a weak absorption band at around 500 nm ($\varepsilon \approx 1 \times 10^3$ M^{-1} cm^{-1}). The former is assigned to mixed ^{1}ILCT and ^{1}MLCT (metal-to-ligand charge-transfer) transitions, while the latter, extending to 600 nm, is tentatively assigned to spin-forbidden ^{3}MLCT/^{3}ILCT transitions in view of the closeness of its energy to its emission. The absorption spectra of **3**–**8** exhibit a [O^N^C^O]-centered π–π* absorption with λ_{max} in the range of 349–366 nm and ILCT absorptions extending to 500 nm (Figure S7A in the Supporting Information). Of note, **6** shows an additional absorption of moderate intensity at 504 nm (ε = 4.2 × 10^3 M^{-1} cm^{-1}), which is tentatively assigned to LLCT/MLCT transitions from O^N^C^O/Ir to the highly electron deficient pyridazine motif.

As depicted in Figure S7B in the Supporting Information, complexes **1**, **3** and **9**, bearing axial MeIm ligands, exhibit the lowest LC π–π* absorption, with energies in the order of **1** (λ_{max} 354 nm) > **3** (λ_{max} 366 nm) > **9** (λ_{max} 368 nm). The lowest LC π–π* absorptions for **2**, **8**, and **14** (Figure S7C) also

follow the trend: **2** (λ_{max} 339 nm) > **8** (λ_{max} 351 nm) > **14** (λ_{max} 367 nm). The progressive bathochromic shift is likely due to the incorporation of the phenyl ring into the [O^N^C^N] ligand, thus extending the π conjugation and electron-donating effects of the ^{t}Bu substituent. Complexes **8** and **15** exhibit similar absorption profiles while the molar absorptivity of **15** is essentially twice that of **8**, which is in agreement with the dinuclear structure of **15**. Similarly, the heteroleptic complexes **19**–**21** show intense [O^N^C^O] π–π* absorptions with λ_{max} in the region of 346–350 nm and moderately intense ILCT/MLCT absorptions at around 400 nm (Figure S7D). It is noteworthy that the [O^N^C^O] π–π* absorptions of **19**–**21** are slightly blue shifted from those of their analogues **3**, **4**, and **7** (357–366 nm), which is likely attributable to the distortion of the [O^N^C^O] ligand plane.

Emission. The luminescent properties of selected complexes in degassed CH$_2$Cl$_2$ (298 K), PMMA film, glassy solution (2-methyltetrahydrofuran, 77 K), and the solid state (298 and 77 K) were examined. The emission data of Ir(III)-O^N^C^O complexes are summarized in Table 1. Complexes **2**, **8**, and **14**, bearing axial NHC ligands, exhibit orange to red (λ_{max} 586–626 nm) emission with quantum yields of 6–12% and lifetimes of 0.1–0.5 μs, in CH$_2$Cl$_2$. The long emission lifetimes reveal their phosphorescent nature. As shown in Figure 7, the emission energies of **2**, **8**, and **14** follow the trend observed for their absorption energies in CH$_2$Cl$_2$ with bathochromic shifts of λ_{max} from 586 nm for **2** to 626 nm for **14**. Taking together the structureless emission profile, the emissions of **2**, **8**, and **14** are assigned to be ^{3}MLCT/^{3}ILCT in nature. The emission of **15** at λ_{max} 581 nm is hypsochromically shifted from that of its mononuclear counterpart **8** (λ_{max} 613 nm); this shift is presumably due to replacing one of the two strong-field NHC ligands that are trans to each other with an oxygen atom donor. In addition, the severely distorted ligand
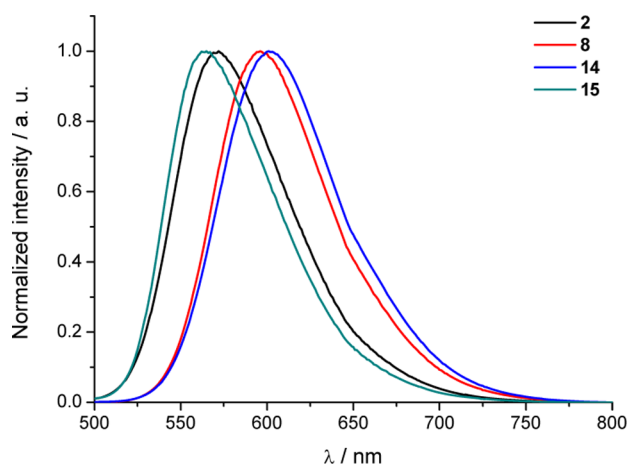
Figure 7. Emission spectra of **2**, **8**, **14**, and **15** in CH_2Cl_2 (4×10^{-5} M; λ_{ex} 365 nm).

scaffold in **15**, as depicted in Figure 3 for its analogue, **16**, is also expected to contribute to the blue-shifted emission.

The emission spectra of complexes **3**, **4**, and **6**−**8** in CH_2Cl_2 are shown in Figure 8. These complexes, bearing the same
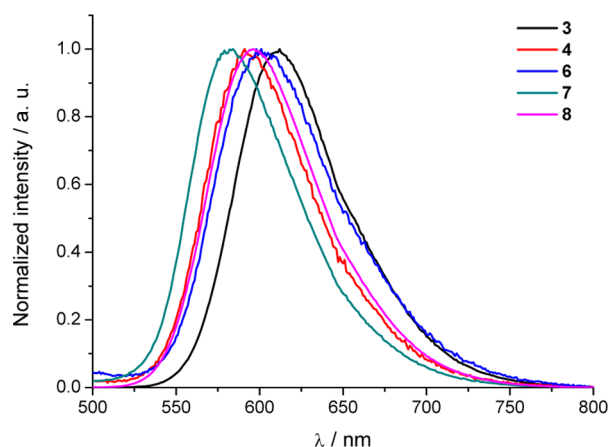

Figure 8. Emission spectra of **3**−**4** and **6**−**8** in CH_2Cl_2 (4×10^{-5} M; λ_{ex} 365 nm).

equatorial ligand **L2**, exhibit emissions with λ_{max} values in the range of 573−626 nm and quantum yields and lifetimes varying with the axial ligands (Table 1). Among these complexes, **3** and **8** display the highest emission quantum yields of 11% and 12%, respectively. The radiative ($k_r = \phi/\tau$) and nonradiative ($k_{nr} = (1 - \phi)/\tau$) decay rate constants for **3** and **4** were estimated on the basis of emission efficiency and lifetime. The k_r values for **3** and **4** are comparable, being 1.7×10^5 and 1.3×10^5 s^{-1}, respectively. The k_{nr} value is 8.5×10^5 s^{-1} for **3**, which is considerably smaller than that of 3.2×10^6 s^{-1} for **4**, suggesting a profound effect of the axial ligand on the nonradiative decay process. Complex **6** exhibits a relatively low emission energy (λ_{max} 622 nm) with a low emission efficiency. Complex **7**, bearing axial PPh$_3$ ligands, affords the highest emission energy (λ_{max} 573 nm), but with the lowest emission efficiency ($\phi <$ 0.1%). The π-accepting phosphine is envisioned to stabilize the Ir d$_\pi$ orbitals, thereby resulting in a blue shift of the emission energy. Significant decreases in emission quantum yields upon using PPh$_3$ ligand(s) has also been reported in luminescent Ir(III) and Pt(II) complexes.[23]

The emissions of the axially heteroleptic complexes **19**−**21** are highly similar to λ_{max} 564 nm (Figure 9). In the cases of **19**
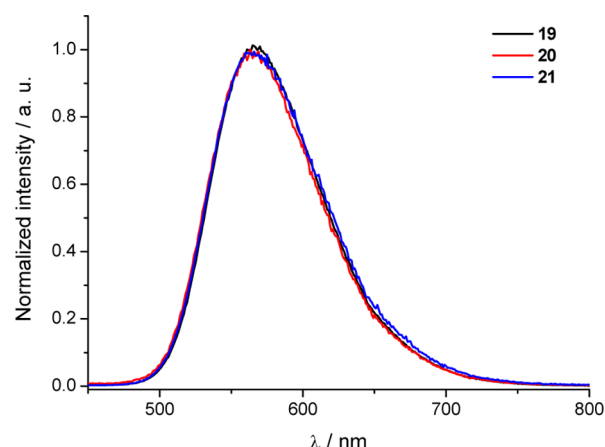

Figure 9. Emission spectra of **19**−**21** in CH_2Cl_2 (4×10^{-5} M; λ_{ex} 365 nm).

and **20**, their emission λ_{max} values are remarkably blue shifted (48−62 nm) in comparison to those of **3** and **4**. This is attributable to the stabilization of the Ir(III) d$_\pi$ orbitals through π back-bonding interactions with the axial isocyanide ligands. In spite of having the same emission energy, complex **21** with axial phosphine ligands displays an emission quantum yield 2 orders of magnitude lower as well as a very short emission lifetime.

Solvent Effect on Photophysical Properties. The absorption and emission spectra of complexes **3**, **4**, and **8** in a panel of solvents were examined. As depicted in Figure 10,
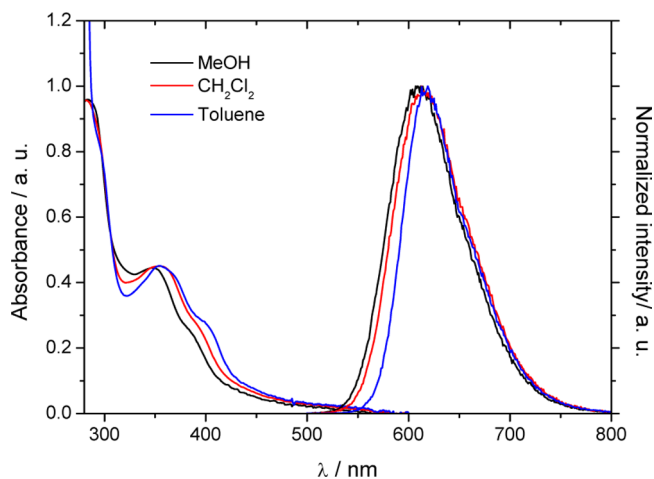
Figure 10. Absorption and emission spectra of **8** in various solvents (2 $\times 10^{-5}$ M).

when the solvent was changed from toluene to methanol the strong absorption of **8** at 400 nm blue-shifts by ∼16 nm. This negative solvatochromic effect is suggestive of charge-transfer character for this transition. Similarly, the emission maximum of **8** displays a blue shift upon increasing the solvent polarity. The solvent-dependent absorption and emission spectra of **3** and **4** exhibit similar solvatochromic behavior (Figure S8 in the Supporting Information).

Emission Properties in PMMA Film. All of the complexes, except **4** and **5**, exhibit significantly enhanced emission quantum yields in PMMA thin film, in comparison to those

in solution (Table 1). Along with the emission quantum yields, the emission lifetimes also increase noticeably. Such findings are attributable to decreased nonradiative decay rate as a result of restricted molecular motion in the rigid solid matrix. In the present cases, the molecular motions that affect the emission properties comprise mainly the excited state $O^\wedge N^\wedge C^\wedge O$ ligand distortion and axial ligand rotation. Suppression of the former will result in blue-shifted emission as well as decreased nonradiative decay by eliminating vibronic crossing between the T_1 and S_0 states. Indeed, thin film emission λ_{max} values of all complexes except **7** are blue-shifted (14−25 nm) in comparison to those in solution (Figure S9 in the Supporting Information). The rigidochromic shift behavior is exemplified by **8** and **19**, as is evident in the data shown in Figure 11. On the other hand,
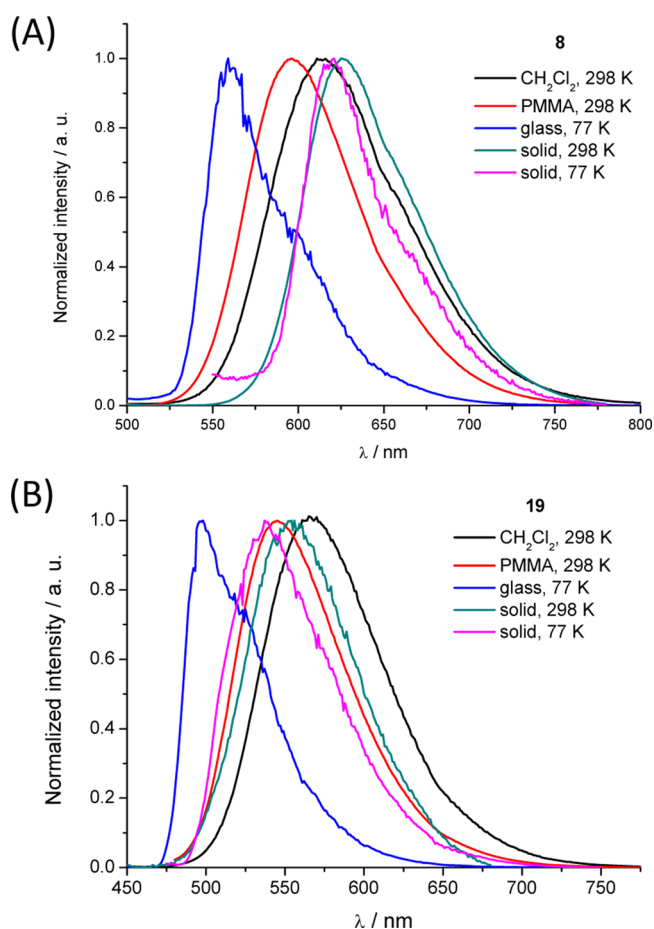

Figure 11. Emission spectra of (A) **8** and (B) **19** in various states.

rotation of the axial ligands provides an efficient channel for depopulating the emitting states. The effect of axial ligands on the emission properties of the present complexes in thin film is also evident. The highest values of 41−51% were recorded for complexes **2**, **8**, and **14**, all of which contain axial NHC ligands. Complexes **7** and **21**, having PPh_3 axial ligands, are also weakly emissive in thin film samples with emission quantum yields of 6% and 1%, respectively.

Solid-State and Glassy-State Emission. The emission spectra of **8** and **19** in glassy 2-methyltetrahydrofuran (2-MeTHF) and in the solid state (298 and 77 K) are presented in Figure 11, and those of the other complexes are given in Figures S10−S13 in the Supporting Information. In 2-MeTHF at 77 K, all complexes show intense phosphorescence with

blue-shifted λ_{max} values and lifetimes significantly prolonged, in comparison to those values measured in solutions at 298 K (Table 1). For example, in the case of **8**, the emission λ_{max} blue shifts from 613 nm (CH_2Cl_2, 298 K) to 559 nm (2-MeTHF, 77 K) and the emission lifetime increases from 0.4 to 3.7 μs. A similar blue shift of 66 nm, along with a 20-fold increase in emission lifetime, has also been found for **19**. The remarkable blue shifts in emission λ_{max} can be attributed to the flexible $O^\wedge N^\wedge C^\wedge O$ ligand scaffold, which undergoes a severe excited-state geometry distortion in solution. Thus, the enhanced emission intensity and increased emission lifetimes in 77 K glassy solutions for all of these Ir-$O^\wedge N^\wedge C^\wedge O$ complexes are due to suppression of excited state geometry distortion. In the solid state at 298 K, all four groups of complexes exhibit weak phosphorescence with lifetimes in the submicrosecond regime. The emission λ_{max} values are close to those recorded in solution (Table 1). Upon cooling to 77 K, these complexes in the solid state display intense emissions accompanied by prolonged emission lifetimes and slight blue shifts in emission λ_{max} (Table 1).

Temperature-Dependent Emission Lifetimes. To shed light on the nonradiative decay pathways of the Ir(III)-$O^\wedge N^\wedge C^\wedge O$ complexes, the emission lifetimes of **3** and **8** in degassed CH_2Cl_2 at variable temperatures (233−293 K) were examined. In this temperature range, identical normalized emission spectra were recorded (Figure S14 in the Supporting Information). The typical pathways for deactivating the T_1 state in this temperature range consist of temperature-independent radiative (k_r) and nonradiative (k_{nr}) pathways and a temperature-dependent nonradiative (NR) channel ($k_{nr}(T)$; Figure 12A).[24] The temperature-independent nonradiative decay
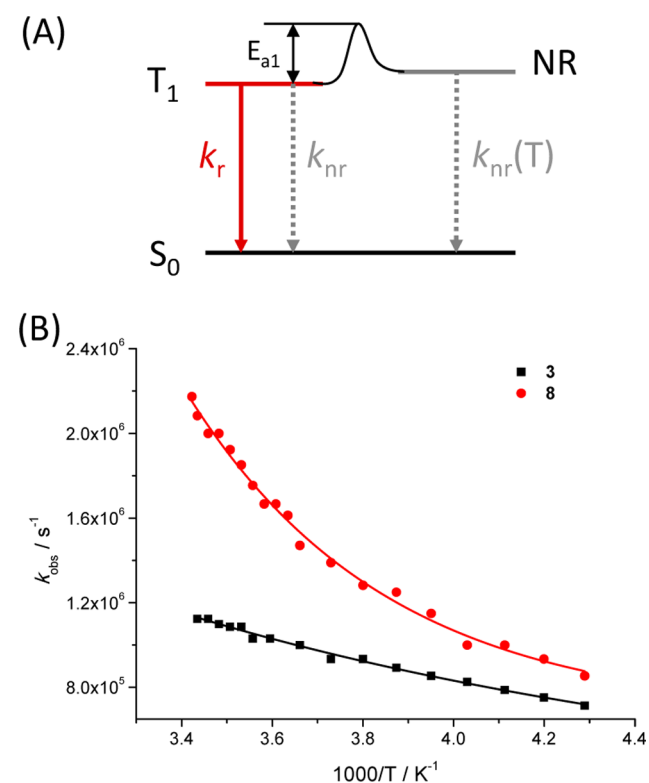

Figure 12. (A) Schematic diagram showing the decay pathways for the T_1 states of the metal complexes. (B) Temperature-dependent k_{obs} values of **3** and **8** in degassed CH_2Cl_2.

pathway is mainly due to the vibronic coupling process between the T_1 and S_0 states. The temperature-dependent nonradiative decay processes are due to thermal population of d–d states and other possible molecular motions which may affect the excited-state dynamics. The emission lifetime is affected by the interplay of these three parameters, as described in eq 1.

$$1/\tau = k_r + k_{nr} + k_1 \exp(-E_{a1}/RT) \quad (1)$$

As depicted in Figure 12B, the emission lifetimes for **3** and **8** decrease with increasing temperature and the temperature dependence agrees well with an Arrhenius relationship. From eq 1, the E_{a1} values for **3** and **8** were found to be 489 and 1578 cm^{-1}, respectively. Given the low emission energies of **3** and **8**, the NR states are unlikely the ligand-field d–d states. The d–d energy levels of a series of cyclometalated Ir(III) complexes have been estimated to lie higher than 20000 cm^{-1} above their ground states.[25] On the other hand, the values of the pre-exponential term k_1 for the dissociative d–d state of Ir(III) complexes are usually in the range of 10^{11}–10^{14} s^{-1},[25] which are strikingly larger than the observed values for **3** ($k_1 = 1.0 \times 10^7$ s^{-1}) and **8** ($k_1 = 3.1 \times 10^9$ s^{-1}). In the present cases, the NR states are probably higher-lying states involving free rotation of the axial ligands. This attribute is supported by the temperature-dependent ^{1}H NMR experiments showing that rotation of the axial NHC ligands of **8** is fast at room temperature but slows down at lower temperatures.

Nanosecond Transient Absorption (ns-TA) and Time-Resolved Emission (ns-TRE) Spectra. The ns-TA and ns-TRE spectra of complexes **3** and **8** in degassed CH$_2$Cl$_2$ following 355 nm laser pulse excitation were recorded. As shown in Figure 13A, the ns-TA of **3** exhibits a broad absorption at 380−800 nm. In addition, a bleaching band corresponding to ground-state absorption at 368 nm was observed. The absorption decay monitored at 413 and 693 nm showed a dominant single-exponential decay behavior with lifetimes of ca. 0.7 μs, which are close to the emission lifetime (0.9 μs; Figure 13B and Figure S15 in the Supporting Information). This suggests that the ns-TA spectrum can be attributed to the T_1 absorption. The ns-TA spectral profile of **8** at 380−800 nm is similar to that of **3**; both feature intense, broad excited state absorption in the visible to near-infrared region (Figure S16 in the Supporting Information).

Comparison with Ir(III)-Corrole Complexes. In 2010, Gray and co-workers reported neutral phosphorescent Ir(III) complexes containing tetradentate trianionic corrole ligands,[12c] which exhibit NIR phosphorescence. However, the emission quantum yields of Ir(III)-corroles are relatively low, with the highest value being only 1.2% in degassed toluene. It is therefore of interest to compare the emission properties of Ir(III)-corroles and Ir(III)-O^N^C^O complexes. On the basis of the emission lifetime data, the k_r values of the Ir(III)-corrole complexes were estimated to be on the order of 10^3 s^{-1}, 2 orders of magnitude lower than those of the Ir(III)-O^N^C^O complexes described in this work as well as most of the other cyclometalated Ir(III) complexes.[11] This is in line with the emissive excited states of Ir(III)-corroles being localized to the corrole ligand. In contrast, the much higher radiative decay rates for the Ir(III)-O^N^C^O complexes are suggestive of decent MLCT character in their emissive excited states, which promotes a spin-forbidden $T_1 \rightarrow S_0$ transition. In addition, the k_{nr} value of 2.0×10^5 s^{-1} for [Ir(corrole)Py$_2$], which was the best emitter reported in Gray's work, is smaller than those of Ir(III)-O^N^C^O complexes ($\sim 10^6$ s^{-1}). It is noteworthy that
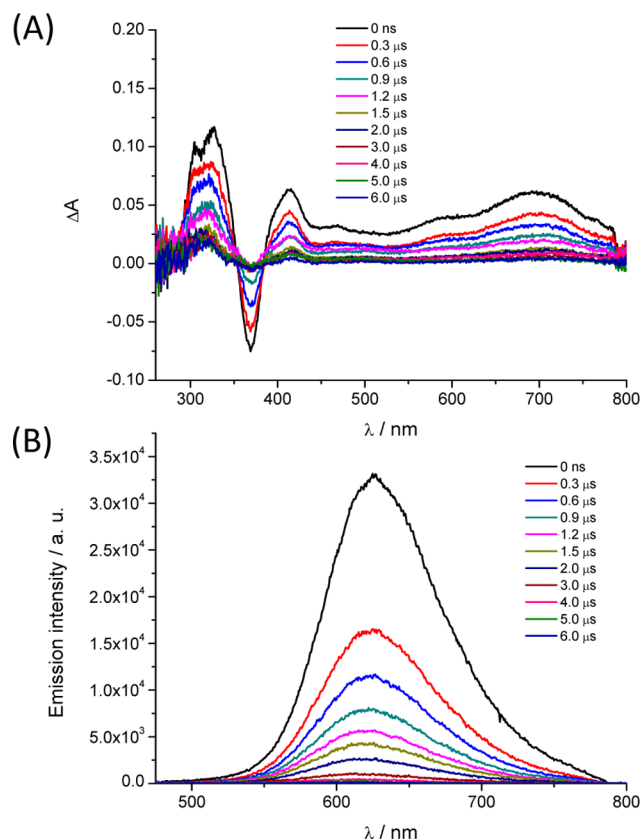

Figure 13. Nanosecond (A) time-resolved absorption (ns-TA) and (B) emission spectra (ns-TRE) of **3** in degassed CH$_2$Cl$_2$ (2×10^{-5} M).

the emission of [Ir(corrole)Py$_2$] in 77 K glassy solution exhibits no blue shift in energy and has a lifetime increased by less than 2-fold in comparison to the values recorded in solutions at room temperature. The lack of a rigidochromic shift in the emission λ_{max} of [Ir(corrole)Py$_2$] is due to the rigidity of the corrole ligand that undergoes minimal geometry distortion in the emissive excited state. This accounts for its slower nonradiative decay rate in comparison to that of the Ir(III)-O^N^C^O complexes.

DFT and TDDFT Calculations. To understand the excited state properties, density functional theory (DFT) and time-dependent density functional theory (TDDFT) calculations were performed on **3**, **4**, and **8**. The optimized S_0 structures of **3**, **4**, and **8** are depicted in Figure S17 in the Supporting Information. The optimized structure of **4** agrees well with its crystal structure (Table S3 in the Supporting Information). The calculated Ir−O, Ir−N, and Ir−C bond lengths and the bite angles are within 0.03 Å and 0.5° deviations from the experimental data. The key structural parameters of the optimized structure of **3** are in good agreement with the crystal structure data of **9**, which should have a structure similar to that of **3**. The plots of selected frontier orbitals of **3**, **4**, and **8** in their respective S_0 states are shown in Figure 14. In all cases the electron density in the HOMO is mainly localized on the Ir d$_\pi$ and π orbitals of the P4 ring with small contributions from the π(P3) orbitals. The LUMO orbital mainly consists of π^* orbitals of the P2 and P5 rings. The significant involvement of the peripheral P5 ring in the LUMO is in line with the observed red shift of absorption and emission λ_{max} values of **3**/**9** and **8**/**14** from those of **1** and **2**, respectively. The simulated
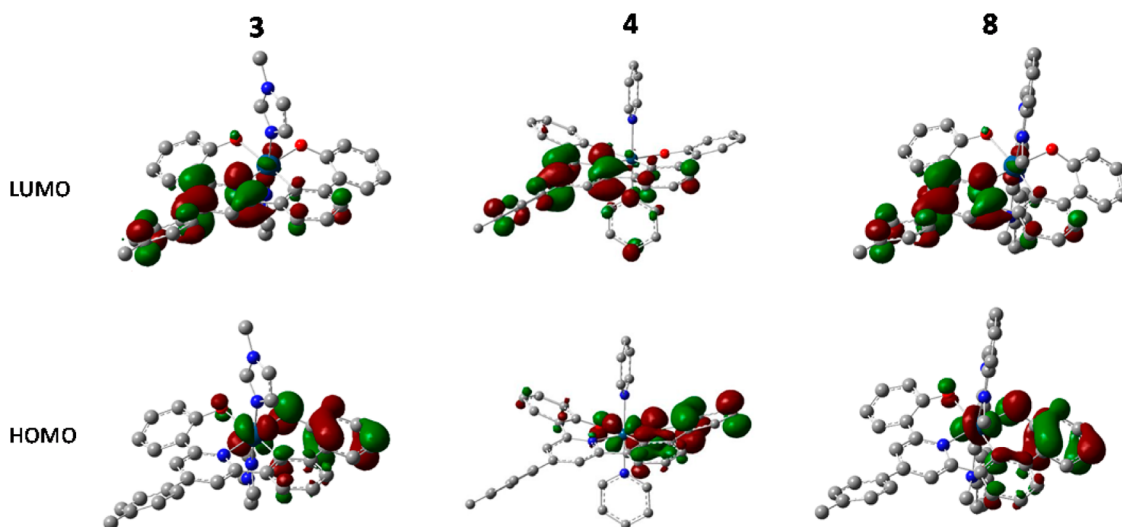
Figure 14. Plots of calculated frontier orbitals of **3**, **4**, and **8** at the optimized S_0 geometry.

absorption profiles for **3** and **8** are in good agreement with the experimentally observed absorption spectra (Figures S18 and S19 in the Supporting Information). As given in Table S4 in the Supporting Information, the lowest energy $S_0 \rightarrow S_1$ absorptions are mainly composed of HOMO → LUMO transitions (94−96% contribution). The calculated $S_0 \rightarrow S_1$ transition energies of 475.6, 466.6, and 466.5 nm for **3**, **4**, and **8**, with relatively small oscillator strength, correspond well to the relatively weak absorption at $\lambda > 450$ nm observed in the absorption spectra of these two complexes. Therefore, the $S_0 \rightarrow S_1$ transitions are intraligand charge transfer (ILCT) combined with a small amount of MLCT character. For **3** and **8**, the higher energy absorptions with strong oscillator strengths mainly involve transitions from the HOMO-1, HOMO-2, or HOMO-3 to LUMO or LUMO+1 orbitals (Table S4). As depicted in Figure S20 in the Supporting Information, all of the orbitals involved are localized to the O^N^C^O ligand, without appreciable involvement of the metal ion or the axial ligands. Therefore, the higher energy absorptions are assigned to O^N^C^O ligand-centered transitions. The assignment is slightly different in the case of **4**; the calculated intense $S_0 \rightarrow S_2$, $S_0 \rightarrow S_4$, $S_0 \rightarrow S_5$, and $S_0 \rightarrow S_6$ transitions at 417, 403, 398, and ~371 nm for **4** are mainly due to transitions involving the HOMO-2, HOMO-1, LUMO, LUMO+1, LUMO+2, and LUMO+3 orbitals. Since the HOMO-1, HOMO, and LUMO of **4** are mainly localized on the O^N^C^O ligand while LUMO+1 is mainly localized on the two axial pyridine ligands, the S_n ($n \geq 2$) states are assigned to have mixed IL and LLCT character.

OLED Performances. Complex **8**, which has the highest emission quantum yield in thin film, was used as a phosphorescent emitter for OLED fabrication. The device structure was ITO/PEDOT:PSS (30 nm)/PYD-2:Ir(III) complex (30 nm)/DEPEO (10 nm)/TPBI (40 nm)/LiF (1.2 nm)/Al (150 nm). The molecular structures of PYD-2, DEPEO, and TPBI are provided in Figure 15A. With increasing Ir(III)-dopant concentration, the electroluminescence (EL) λ_{max} slightly red shifted, presumably as the result of intermolecular $\pi-\pi$ interactions (Figure 15B). The EL spectrum was stable in the operational voltage range of 7−12 V. The CIE chromaticity coordinates of (0.64, 0.36) for the devices with **8** at 12 and 20 wt % doping levels revealed the complex to be a promising red emitter. The external quantum

efficiency (EQE) values of the devices are shown in Figure 15C, and the performance data are given in Table 2. The best device performance was obtained using **8** at a doping concentration of 12 wt % with a maximum current efficiency of 12.9 cd A^{-1} and an EQE of 10.5%. Such an EQE is among the high values for solution-processed red phosphorescent OLEDs.[26] However, the maximum brightness was only thousands of cd m^{-2} and the devices exhibited severe efficiency rolloff at high brightness. For example, the EQE of the device doped with **8** dropped from 10.5% to 5.3% at a brightness of 1000 cd m^{-2}. These characteristics are attributable to emission self-quenching effect.

■ CONCLUSION

A new type of tetradentate trianionic O^N^C^O ligand was developed and used for the preparation of Ir(III) complexes. A library of new Ir-O^N^C^O complexes bearing different neutral axial ligands was synthesized and examined with a suite of spectroscopic techniques. The complexes containing axial NHC ligands undergo slow dimerization in CH$_2$Cl$_2$, resulting in μ-O-bridged dinuclear complexes. The dimerization is likely caused by the strong mutual trans influence of the NHC ligands. Although the emissive excited states of these Ir-O^N^C^O complexes are mainly ^{3}ILCT/^{3}MLCT in nature with L = O^N^C^O, the axial ligands have been shown to exert profound effects on the luminescent properties of the complexes, presumably through stabilizing the Ir dπ orbitals and affecting nonradiative decay rates. The complexes containing axial NHC ligands show superior emission properties in both degassed solutions and PMMA films at room temperature. Temperature-dependent emission lifetime experiments suggest that, in the cases of **3** and **8**, there are closely high-lying nonradiative states above the emitting T$_1$ states, which could be attributed to the rotation of the axial ligands. Efficient red OLEDs have been fabricated with a high EQE of 10.5% by using **8** as the emitter. This novel tetradentate trianionic O^N^C^O-type ligand system, complementary to the well-documented systems featuring combinations of bidentate and/or tridentate ligands, is conceived to provide access to a new class of phosphorescent Ir(III) complexes with tunable photophysical and luminescent properties.
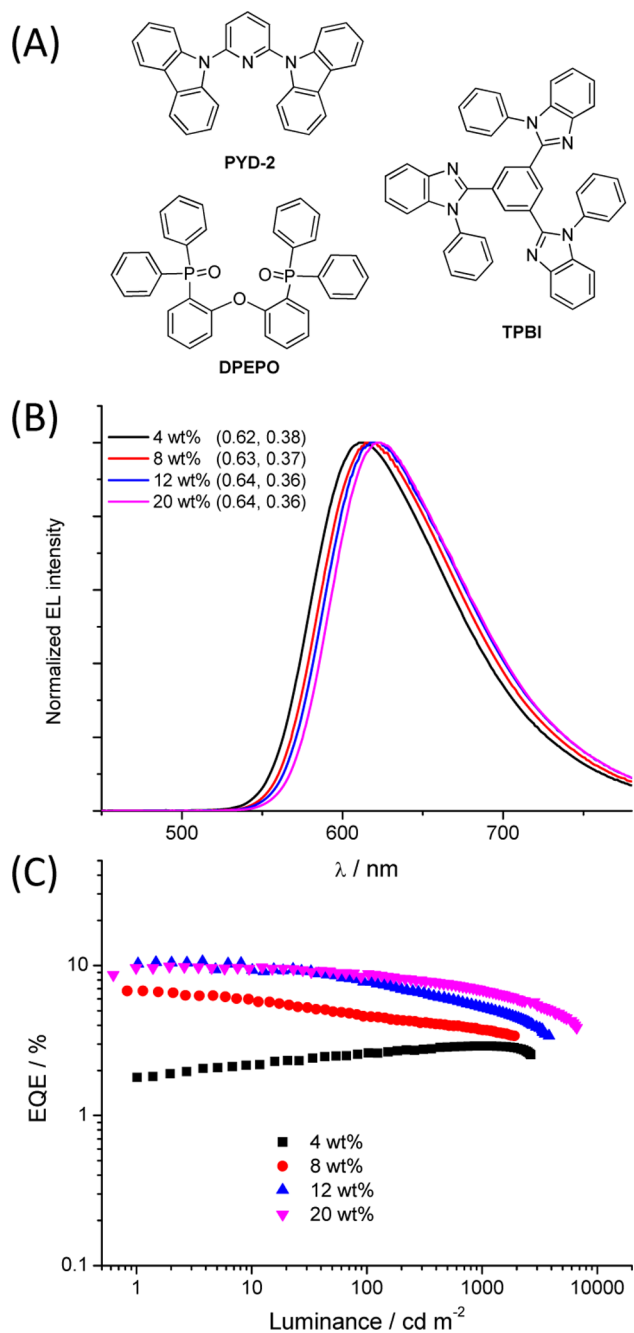
Figure 15. (A) Structures of PYD-2, TPBI, and DPEPO used in OLED fabrication. (B) Normalized EL spectra of the devices doped with **8** at 100 cd m^{-2}. (C) EQE of the devices doped with **8** vs luminance.

Table 2. Electroluminescence Performances of OLEDs Doped with 8

concentration (wt %)	max luminance (cd m^{-2})	current efficiency (cd A^{-1})		EQE (%)	
		max	@ 1000 cd m^{-2}	max	@ 1000 cd m^{-2}
4	2650	4.07	4.07	2.92	2.92
8	2910	8.34	4.59	6.78	3.73
12	3390	12.92	6.46	10.49	5.25
20	5410	10.12	7.20	9.64	6.86

■ EXPERIMENTAL SECTION

Materials and Reagents. All materials were purchased from commercial sources and were used without further purification, unless otherwise indicated. [Ir(Cod)Cl]$_2$ was prepared from IrCl$_3$·xH$_2$O and cyclooctadiene. Palladium-catalyzed coupling reactions were used for preparing ligands **H$_3$L1**–**H$_3$L3**. Dry THF was freshly distilled from sodium−benzophenone.

Physical Measurements and Instrumentation. The solvents used for photophysical measurements were of HPLC grade. Elemental analyses were performed by the Institute of Chemistry at the Chinese Academy of Sciences, Beijing, People's Republic of China. Fast atom bombardment (FAB) mass spectra were obtained on a Finnigan Mat 95 mass spectrometer. Electrospray ionization (ESI) mass spectra were collected on a Finnigan LCQ quadrupole ion trap mass spectrometer (samples were dissolved in HPLC grade solvent). ^{1}H, ^{19}F, and ^{31}P NMR spectra were recorded on DPX300 and Avance400 Bruker FT-NMR spectrometers. UV−vis absorption spectra were recorded on a PerkinElmer Lambda 19 UV/vis spectrophotometer. Steady-state emission spectra at 298 K were obtained on a Spex 1681 Fluorolog-2 Model F111 spectrophotometer equipped with a Hamamatsu R928 PMT detector. All solutions for photophysical measurements, except as stated otherwise, were degassed in a high-vacuum line with at least four freeze−pump−thaw cycles. Emission lifetimes were measured with a Quanta-Ray Q-switch DCR-3 Nd:YAG pulsed laser system. Emission quantum yields of solutions were measured using a degassed acetonitrile solution of [Ru(bpy)$_3$](PF$_6$)$_2$ (bpy = 2,2′-bipyridine) (ϕ_r = 0.062) as the standard. Errors for ϕ (10%) are estimated. The nanosecond time-resolved absorption difference spectra (ns-TA) and nanosecond time-resolved emission spectra (ns-TRE) were performed with a LP920-KS Laser Flash Photolysis Spectrometer (Edinburgh Instruments Ltd., Livingston, U.K.). The excitation source was the 355 nm output (third harmonic) of an Nd:YAG laser (Spectra-Physics Quanta-Ray Lab-130 pulsed Nd:YAG laser). The signals were processed by a PC plugin controlled with L900 software. Cyclic voltammetric measurements were performed with a Princeton Applied Research electrochemical analyzer (potentiostat/galvanostat Model 273A). ^{n}Bu$_4$NPF$_6$ (0.1 M) in CH$_2$Cl$_2$ was used as a supporting electrolyte for the electrochemical measurements at room temperature. All solutions used in electrochemical measurements were deaerated with argon gas. Ag/AgNO$_3$ (0.1 M in MeCN), a glassy-carbon electrode, and a platinum wire were used as reference electrode, working electrode, and counter electrode, respectively. The ferrocenium/ferrocene (Cp$_2$Fe$^{+/0}$) redox couple was used as an internal reference.

X-ray Diffraction Measurements. The X-ray diffraction data were collected on a Bruker X8 PROTEUM single-crystal X-ray diffractometer. Raw frame data were integrated using the SAINT program. Multiscan SADABS was applied for absorption correction. The structures were solved by using Olex2[27] software with employing the ShelXS[28] structure solution program by direct methods and refined with the ShelXL[29] refinement package using least-squares minimization. The positions of the hydrogen atoms were calculated on the basis of the riding mode with thermal parameters equal to 1.2 and 1.5 times that of the associated C atoms and terminal methyl groups, and these positions participated in the calculation of the final R indices. In the final stage of least-squares refinement, all non-hydrogen atoms were refined anisotropically.

Computational Methods. The density functional theory (DFT) and time-dependent density functional theory (TDDFT) calculations for complexes **3**, **4**, and **8** were carried out using the PBE0 functional[30] with a basis set of 6-31+G*[31] for the C, H, and N atoms and a pseudopotential Stuttgart/Dresden (SDD)[32] basis set for the Ir atom. Solvent effects were examined using the self-consistent reaction field (SCRF) method based on PCM models.[33] The Gaussian 09 package was used for the calculations.[34]

■ ASSOCIATED CONTENT

S Supporting Information

this material is available free of charge via the Internet at The Supporting Information is available free of charge on the ACS Publications website at DOI: 10.1021/acs.organomet.7b00038.

> Synthesis and characterization data of the ligands and complexes, crystal data and selected bond distances and bond angles, crystal structures, absorption and emission spectra of selected complexes, and DFT optimized structures and TDDFT calculated transition energies for **3**, **4**, and **8** (PDF)
> Crystallographic data (CIF)

■ AUTHOR INFORMATION

Corresponding Author
*E-mail for C.-M.C.: cmche@hku.hk.

ORCID ⊙
Kai Li: 0000-0002-5869-1006

Author Contributions
§D.C. and K.L. contributed equally.

Notes
The authors declare no competing financial interest.

■ ACKNOWLEDGMENTS

■ REFERENCES

(1) Selected reviews for metalloporphyrin catalysts: (a) Meunier, B. *Chem. Rev.* **1992**, *92*, 1411−1456. (b) Bedioui, F. *Coord. Chem. Rev.* **1995**, *144*, 39−68. (c) Dolphin, D.; Traylor, T. G.; Xie, L. Y. *Acc. Chem. Res.* **1997**, *30*, 251−259. (d) Simonneaux, G.; Le Maux, P. *Coord. Chem. Rev.* **2002**, *228*, 43−60. (e) Rose, E.; Andrioletti, B.; Zrig, S.; Quelquejeu-Ehtève, M. *Chem. Soc. Rev.* **2005**, *34*, 573−583. (f) Mansuy, D. *C. R. Chim.* **2007**, *10*, 392−413. (g) Shinokubo, H.; Osuka, A. *Chem. Commun.* **2009**, 1011−1021. (h) Che, C.-M.; Huang, J.-S. *Chem. Commun.* **2009**, 3996−4015. (i) Lu, H. J.; Zhang, X. P. *Chem. Soc. Rev.* **2011**, *40*, 1899−1909. (j) Che, C.-M.; Lo, V. K.-Y.; Zhou, C.-Y.; Huang, J.-S. *Chem. Soc. Rev.* **2011**, *40*, 1950−1975. (k) Costas, M. *Coord. Chem. Rev.* **2011**, *255*, 2912−2932. (l) Costentin, C.; Robert, M.; Savéant, J.-M. *Acc. Chem. Res.* **2015**, *48*, 2996−3006. (m) Rybicka-Jasińska, K.; Ciszewski, Ł. W.; Gryko, D. T.; Gryko, D. *J. Porphyrins Phthalocyanines* **2016**, *20*, 76−95. (n) Intrieri, D.; Carminati, D. M.; Gallo, E. *J. Porphyrins Phthalocyanines* **2016**, *20*, 190−203.

(2) Selected reviews for metal catalysts bearing planar tetradentate Schiff base ligands: (a) Katsuki, T. *Coord. Chem. Rev.* **1995**, *140*, 189−214. (b) Dalton, C. T.; Ryan, K. M.; Wall, V. M.; Bousquet, C.; Gilheany, D. G. *Top. Catal.* **1998**, *5*, 75−91. (c) Canali, L.; Sherrington, D. C. *Chem. Soc. Rev.* **1999**, *28*, 85−93. (d) Atwood, D. A.; Harvey, M. J. *Chem. Rev.* **2001**, *101*, 37−52. (e) Cozzi, P. G. *Chem. Soc. Rev.* **2004**, *33*, 410−421. (f) Darensbourg, D. J.; Mackiewicz, R. M.; Phelps, A. L.; Billodeaux, D. R. *Acc. Chem. Res.* **2004**, *37*, 836−844. (g) Irie, R.; Katsuki, T. *Chem. Rec.* **2004**, *4*, 96−109. (h) Achard, T. R. J.; Clutterbuck, L. A.; North, M. *Synlett* **2005**, 1828−1847. (i) Venkataraman, N. S.; Kuppuraj, G.; Rajagopal, S. *Coord. Chem. Rev.* **2005**, *249*, 1249−1268. (j) Baleizão, C.; Garcia, H. *Chem. Rev.* **2006**, *106*, 3987−4043. (k) Darensbourg, D. J. *Chem. Rev.*

2007, *107*, 2388−2410. (l) Gupta, K. C.; Sutar, A. K. *Coord. Chem. Rev.* **2008**, *252*, 1420−1450. (m) Kleij, A. W. *Eur. J. Inorg. Chem.* **2009**, *2009*, 193−205. (n) Decortes, A.; Castilla, A. M.; Kleij, A. W. *Angew. Chem., Int. Ed.* **2010**, *49*, 9822−9837. (o) Vigato, P. A.; Peruzzo, V.; Tamburini, S. *Coord. Chem. Rev.* **2012**, *256*, 953−1114. (p) Matsunaga, S.; Shibasaki, M. *Synthesis* **2013**, *45*, 421−437. (q) Al Zoubi, W.; Ko, Y. G. *J. Organomet. Chem.* **2016**, *822*, 173−188. (r) Das, P.; Linert, W. *Coord. Chem. Rev.* **2016**, *311*, 1−23.

(3) Selected reviews for application of metalloporphyrins in materials science: (a) Calvete, M.; Yang, G. Y.; Hanack, M. *Synth. Met.* **2004**, *141*, 231−243. (b) Elemans, J. A. A. W.; van Hameren, R.; Nolte, R. J. M.; Rowan, A. E. *Adv. Mater.* **2006**, *18*, 1251−1266. (c) Takagi, S.; Eguchi, M.; Tryk, D. A.; Inoue, H. *J. Photochem. Photobiol., C* **2006**, *7*, 104−126. (d) Senge, M. O.; Fazekas, M.; Notaras, E. G. A.; Blau, W. J.; Zawadzka, M.; Locos, O. B.; Mhuircheartaigh, E. M. N. *Adv. Mater.* **2007**, *19*, 2737−2774. (e) Drain, C. M.; Varotto, A.; Radivojevic, I. *Chem. Rev.* **2009**, *109*, 1630−1658. (f) Amao, Y.; Okura, I. *J. Porphyrins Phthalocyanines* **2009**, *13*, 1111−1122. (g) Jurow, M.; Schuckman, A. E.; Batteas, J. D.; Drain, C. M. *Coord. Chem. Rev.* **2010**, *254*, 2297−2310. (h) Panda, M. K.; Ladomenou, K.; Coutsolelos, A. G. *Coord. Chem. Rev.* **2012**, *256*, 2601−2627. (i) Carvalho, C. M. B.; Brocksom, T. J.; de Oliveira, K. T. *Chem. Soc. Rev.* **2013**, *42*, 3302−3317. (j) Li, L.-L.; Diau, E. W.-G. *Chem. Soc. Rev.* **2013**, *42*, 291−304. (k) Gao, W.-Y.; Chrzanowski, M.; Ma, S. *Chem. Soc. Rev.* **2014**, *43*, 5841−5866. (l) Urbani, M.; Grätzel, M.; Nazeeruddin, M. K.; Torres, T. *Chem. Rev.* **2014**, *114*, 12330−12396. (m) Auwärter, W.; Écija, D.; Klappenberger, F.; Barth, J. V. *Nat. Chem.* **2015**, *7*, 105−120. (n) Tanaka, T.; Osuka, A. *Chem. Soc. Rev.* **2015**, *44*, 943−969. (o) Chakraborty, J.; Nath, I.; Verpoort, F. *Coord. Chem. Rev.* **2016**, *326*, 135−163.

(4) Selected reviews for application of metal complexes bearing planar tetradentate Schiff base ligands in materials science: (a) Miyasaka, H.; Saitoh, A.; Abe, S. *Coord. Chem. Rev.* **2007**, *251*, 2622−2664. (b) Wezenberg, S. J.; Kleij, A. W. *Angew. Chem., Int. Ed.* **2008**, *47*, 2354−2364. (c) Dalla Cort, A.; De Bernardin, P.; Forte, G.; Mihan, F. Y. *Chem. Soc. Rev.* **2010**, *39*, 3863−3874. (d) Crane, A. K.; MacLachlan, M. J. *Eur. J. Inorg. Chem.* **2012**, *2012*, 17−30.

(5) Selected reviews: (a) Patel, M.; Day, B. J. *Trends Pharmacol. Sci.* **1999**, *20*, 359−364. (b) Sun, R. W.-Y.; Che, C.-M. *Coord. Chem. Rev.* **2009**, *253*, 1682−1691. (c) Sheng, H.; Chaparro, R. E.; Sasaki, T.; Izutsu, M.; Pearlstein, R. D.; Tovmasyan, A.; Warner, D. S. *Antioxid. Redox Signaling* **2014**, *20*, 2437−2464. (d) Singh, S.; Aggarwal, A.; Bhupathiraju, N. V.; Arianna, G.; Tiwari, K.; Drain, C. M. *Chem. Rev.* **2015**, *115*, 10261−10306.

(6) Selected reviews: (a) Uchida, T.; Katsuki, T. *Chem. Rec.* **2014**, *14*, 117−129. (b) Schafer, A. G.; Blakey, S. B. *Chem. Soc. Rev.* **2015**, *44*, 5969−5980.

(7) Koren, K.; Borisov, S. M.; Saf, R.; Klimant, I. *Eur. J. Inorg. Chem.* **2011**, *2011*, 1531−1534.

(8) (a) Che, C.-M.; Cheng, W.-K.; Leung, W.-H.; Mak, T. C. W. *J. Chem. Soc., Chem. Commun.* **1987**, 418−419. (b) Chan, P.-M.; Yu, W.-Y.; Che, C.-M.; Cheung, K.-K. *J. Chem. Soc., Dalton Trans.* **1998**, 3183−3190. (c) Yip, K.-L.; Yu, W.-Y.; Chan, P.-M.; Zhu, N.-Y.; Che, C.-M. *Dalton Trans.* **2003**, 3556−3566.

(9) Selected reviews: (a) Gryko, D. T.; Fox, J. P.; Goldberg, D. P. *J. Porphyrins Phthalocyanines* **2004**, *08*, 1091−1105. (b) Aviv, I.; Gross, Z. *Chem. Commun.* **2007**, 1987−1999. (c) Aviv-Harel, I.; Gross, Z. *Chem. - Eur. J.* **2009**, *15*, 8382−8394. (d) Flamigni, L.; Gryko, D. T. *Chem. Soc. Rev.* **2009**, *38*, 1635−1646. (e) Aviv-Harel, I.; Gross, Z. *Coord. Chem. Rev.* **2011**, *255*, 717−736. (f) Palmer, J. H. In *Molecular Electronic Structures of Transition Metal Complexes I*; Mingos, D. M. P., Day, P., Dahl, J. P., Eds.; Springer: New York, 2012; Vol. 142, pp 49−89. (g) Thomas, K. E.; Alemayehu, A. B.; Conradie, J.; Beavers, C. M.; Ghosh, A. *Acc. Chem. Res.* **2012**, *45*, 1203−1214. (h) Liu, H.-Y.; Mahmood, M. H. R.; Qiu, S.-X.; Chang, C. K. *Coord. Chem. Rev.* **2013**, *257*, 1306−1333. (i) König, M.; Faschinger, F.; Reith, L. M.; Schöfberger, W. *J. Porphyrins Phthalocyanines* **2016**, *20*, 96−107. (j) Barata, J. F. B.; Neves, M. G. P. M. S.; Faustino, M. A. F.; Tomé, A. C.; Cavaleiro, J. A. S. *Chem. Rev.* **2017**, *117*, 3192.

(10) For examples, see: (a) Kim, H.; Burghart, A.; Welch, M. B.; Reibenspies, J.; Burgess, K. *Chem. Commun.* **1999**, 1889−1890. (b) Ikeda, C.; Ueda, S.; Nabeshima, T. *Chem. Commun.* **2009**, 2544−2546. (c) Rausaria, S.; Kamadulski, A.; Rath, N. P.; Bryant, L.; Chen, Z.; Salvemini, D.; Neumann, W. L. *J. Am. Chem. Soc.* **2011**, *133*, 4200−4203. (d) Sakamoto, N.; Ikeda, C.; Yamamura, M.; Nabeshima, T. *J. Am. Chem. Soc.* **2011**, *133*, 4726−4729. (e) El Ghachtouli, S.; Wojcik, K.; Copey, L.; Szydlo, F.; Framery, E.; Goux-Henry, C.; Billon, L.; Charlot, M.-F.; Guillot, R.; Andrioletti, B.; Aukauloo, A. *Dalton Trans.* **2011**, *40*, 9090−9093. (f) Nakano, K.; Kobayashi, K.; Nozaki, K. *J. Am. Chem. Soc.* **2011**, *133*, 10720−10723. (g) Kochem, A.; Chiang, L.; Baptiste, B.; Philouze, C.; Leconte, N.; Jarjayes, O.; Storr, T.; Thomas, F. *Chem. - Eur. J.* **2012**, *18*, 14590−14593. (h) Yamamura, M.; Albrecht, M.; Albrecht, M.; Nishimura, Y.; Arai, T.; Nabeshima, T. *Inorg. Chem.* **2014**, *53*, 1355. (i) Ohkawara, T.; Suzuki, K.; Nakano, K.; Mori, S.; Nozaki, K. *J. Am. Chem. Soc.* **2014**, *136*, 10728−10735. (j) Feng, Y.; Burns, L. A.; Lee, L.-C.; Sherrill, C. D.; Jones, C. W.; Murdock, C. *Inorg. Chim. Acta* **2015**, *430*, 30−35. (k) Saikawa, M.; Daicho, M.; Nakamura, T.; Uchida, J.; Yamamura, M.; Nabeshima, T. *Chem. Commun.* **2016**, *52*, 4014−4017. (l) Lecarme, L.; Chiang, L.; Moutet, J.; Leconte, N.; Philouze, C.; Jarjayes, O.; Storr, T.; Thomas, F. *Dalton Trans.* **2016**, *45*, 16325−16334.

(11) Selected reviews: (a) Williams, J. A. G. *Chem. Soc. Rev.* **2009**, *38*, 1783−1801. (b) Ulbricht, C.; Beyer, B.; Friebe, C.; Winter, A.; Schubert, U. S. *Adv. Mater.* **2009**, *21*, 4418−4441. (c) Wong, W.-Y.; Ho, C.-L. *Coord. Chem. Rev.* **2009**, *253*, 1709−1758. (d) Liu, Z.; Bian, Z.; Huang, C. *Top. Organomet. Chem.* **2010**, *28*, 113−142. (e) Chi, Y.; Chou, P.-T. *Chem. Soc. Rev.* **2010**, *39*, 638−655. (f) Zhou, G. J.; Wong, W. Y.; Yang, X. L. *Chem. - Asian J.* **2011**, *6*, 1706−1727. (g) Lo, K. K.-W.; Li, S. P.-Y.; Zhang, K. Y. *New J. Chem.* **2011**, *35*, 265−287. (h) Xiao, L.; Chen, Z.; Qu, B.; Luo, J.; Kong, S.; Gong, Q.; Kido, J. *Adv. Mater.* **2011**, *23*, 926−952. (i) Guerchais, V.; Fillaut, J.-L. *Coord. Chem. Rev.* **2011**, *255*, 2448−2457. (j) You, Y.; Nam, W. *Chem. Soc. Rev.* **2012**, *41*, 7061−7084. (k) Xu, H.; Chen, R.; Sun, Q.; Lai, W.; Su, Q.; Huang, W.; Liu, X. *Chem. Soc. Rev.* **2014**, *43*, 3259−3302. (l) Fan, C.; Yang, C. L. *Chem. Soc. Rev.* **2014**, *43*, 6439−6469. (m) Yang, X.; Zhou, G.; Wong, W.-Y. *Chem. Soc. Rev.* **2015**, *44*, 8484−8575. (n) Omae, I. *Coord. Chem. Rev.* **2016**, *310*, 154−169. (o) Chi, Y.; Chang, T.-K.; Ganesan, P.; Rajakannu, P. *Coord. Chem. Rev.* **2016**, DOI: 10.1016/j.ccr.2016.11.016.

(12) (a) Palmer, J. H.; Day, M. W.; Wilson, A. D.; Henling, L. M.; Gross, Z.; Gray, H. B. *J. Am. Chem. Soc.* **2008**, *130*, 7786. (b) Palmer, J. H.; Mahammed, A.; Lancaster, K. M.; Gross, Z.; Gray, H. B. *Inorg. Chem.* **2009**, *48*, 9308. (c) Palmer, J. H.; Durrell, A. C.; Gross, Z.; Winkler, J. R.; Gray, H. B. *J. Am. Chem. Soc.* **2010**, *132*, 9230−9231.

(13) (a) Palmer, J. H.; Brock-Nannestad, T.; Mahammed, A.; Durrell, A. C.; VanderVelde, D.; Virgil, S.; Gross, Z.; Gray, H. B. *Angew. Chem., Int. Ed.* **2011**, *50*, 9433−9436. (b) Sinha, W.; Ravotto, L.; Ceroni, P.; Kar, S. *Dalton Trans.* **2015**, *44*, 17767−17773. (c) Chen, W.; Zhang, J.; Mack, J.; Kubheka, G.; Nyokong, T.; Shen, Z. *RSC Adv.* **2015**, *5*, 50962−50967.

(14) Maurya, Y. K.; Ishikawa, T.; Kawabe, Y.; Ishida, M.; Toganoh, M.; Mori, S.; Yasutake, Y.; Fukatsu, S.; Furuta, H. *Inorg. Chem.* **2016**, *55*, 6223−6230.

(15) Adiraju, V. A. K.; Ferrence, G. M.; Lash, T. D. *Dalton Trans.* **2016**, *45*, 13691−13694.

(16) Wong, B. Y.-W.; Wong, H.-L.; Wong, Y.-C.; Chan, M.-Y.; Yam, V. W.-W. *Angew. Chem., Int. Ed.* **2017**, *56*, 302−305.

(17) (a) Kui, S. C. F.; Chow, P. K.; Tong, G. S. M.; Lai, S.-L.; Cheng, G.; Kwok, C.-C.; Low, K.-H.; Ko, M. Y.; Che, C.-M. *Chem. - Eur. J.* **2013**, *19*, 69−73. (b) Kui, S. C. F.; Chow, P. K.; Cheng, G.; Kwok, C.-C.; Kwong, C. L.; Low, K.-H.; Che, C.-M. *Chem. Commun.* **2013**, *49*, 1497−1499. (c) Cheng, G.; Chow, P.-K.; Kui, S. C. F.; Kwok, C.-C.; Che, C.-M. *Adv. Mater.* **2013**, *25*, 6765−6770. (d) Cheng, G.; Kui, S. C. F.; Ang, W.-H.; Ko, M.-Y.; Chow, P.-K.; Kwong, C.-L.; Kwok, C.-C.; Ma, C.; Guan, X.; Low, K.-H.; Su, S.-J.; Che, C.-M. *Chem. Sci.* **2014**, *5*, 4819−4830. (e) Lai, S.-L.; Tong, W.-Y.; Kui, S. C. F.; Chan, M.-Y.; Kwok, C.-C.; Che, C.-M. *Adv. Funct. Mater.* **2013**, *23*, 5168−5176. (f) Li, K.; Tong, G. S. M; Wan, Q.; Cheng, G.; Tong, W.-Y.;

Ang, W.-H.; Kwong, W.-L.; Che, C.-M. *Chem. Sci.* **2016**, *7*, 1653−1673.

(18) (a) Chow, P. K.; Ma, C.; To, W.-P.; Tong, G. S. M.; Lai, S.-L.; Kui, S. C. F.; Kwok, W.-M.; Che, C.-M. *Angew. Chem., Int. Ed.* **2013**, *52*, 11775−11779. (b) Chow, P.-K.; Cheng, G.; Tong, G. S. M.; Ma, C.; Kwok, W.-M.; Ang, W.-H.; Chung, C. Y.-S.; Yang, C.; Wang, F.; Che, C.-M. *Chem. Sci.* **2016**, *7*, 6083−6098.

(19) Wong, C.-Y.; Man, W.-L.; Wang, C.; Kwong, H.-L.; Wong, W.-Y.; Lau, T.-C. *Organometallics* **2008**, *27*, 324−326.

(20) Stynes, D. V. *Inorg. Chem.* **1977**, *16*, 1170−1173.

(21) Chen, J.-T.; Chen, Y.-K.; Chu, J.-B.; Lee, G.-H.; Wang, Y. *Organometallics* **1997**, *16*, 1476−1483.

(22) (a) Chianese, A. R.; Mo, A.; Lampland, N. L.; Swartz, R. L.; Bremer, P. T. *Organometallics* **2010**, *29*, 3019−3026. (b) Yang, C.-H.; Beltran, J.; Lemaur, V.; Cornil, J.; Hartmann, D.; Sarfert, W.; Fröhlich, R.; Bizzarri, C.; De Cola, L. *Inorg. Chem.* **2010**, *49*, 9891−9901. (c) Navarro, J.; Torres, O.; Martín, M.; Sola, E. *J. Am. Chem. Soc.* **2011**, *133*, 9738−9740. (d) Phillips, N.; Rowles, J.; Kelly, M. J.; Riddlestone, I.; Rees, N. H.; Dervisi, A.; Fallis, I. A.; Aldridge, S. *Organometallics* **2012**, *31*, 8075−8078. (e) Gülcemal, D.; Gülcemal, S.; Robertson, C. M.; Xiao, J. *Organometallics* **2015**, *34*, 4394−4400.

(23) (a) Kui, S. C. F.; Sham, I. H. T.; Cheung, C. C. C.; Ma, C.-W.; Yan, B.; Zhu, N.; Che, C.-M.; Fu, W.-F. *Chem. - Eur. J.* **2007**, *13*, 417−435. (b) Chiu, Y.-C.; Hung, J.-Y.; Chi, Y.; Chen, C.-C.; Chang, C.-H.; Wu, C.-C.; Cheng, Y.-M.; Yu, Y.-C.; Lee, G.-H.; Chou, P.-T. *Adv. Mater.* **2009**, *21*, 2221−2225. (c) Prokhorov, A. M.; Hofbeck, T.; Czerwieniec, R.; Suleymanova, A. F.; Kozhevnikov, D. N.; Yersin, H. *J. Am. Chem. Soc.* **2014**, *136*, 9637−9642. (d) Sanning, J.; Ewen, P. R.; Stegemann, L.; Schmidt, J.; Daniliuc, C. G.; Koch, T.; Doltsinis, N. L.; Wegner, D.; Strassert, C. A. *Angew. Chem., Int. Ed.* **2015**, *54*, 786−791.

(24) (a) Van Houten, J.; Watts, R. J. *J. Am. Chem. Soc.* **1976**, *98*, 4853−4858. (b) Durham, B.; Caspar, J. V.; Nagle, J. K.; Meyer, T. J. *J. Am. Chem. Soc.* **1982**, *104*, 4803−4810.

(25) Sajoto, T.; Djurovich, P. I.; Tamayo, A. B.; Oxgaard, J.; Goddard, W. A.; Thompson, M. E. *J. Am. Chem. Soc.* **2009**, *131*, 9813−9822.

(26) (a) Ho, C.-L.; Wong, W.-Y.; Gao, Z.-Q.; Chen, C.-H.; Cheah, K.-W.; Yao, B.; Xie, Z.; Wang, Q.; Ma, D.; Wang, L.; Yu, X.-M.; Kwok, H.-S.; Lin, Z. *Adv. Funct. Mater.* **2008**, *18*, 319−331. (b) Ding, J.; Lü, J.; Cheng, Y.; Xie, Z.; Wang, L.; Jing, X.; Wang, F. *Adv. Funct. Mater.* **2008**, *18*, 2754−2762. (c) Lee, S.-J.; Park, J.-S.; Song, M.; Shin, I. A.; Kim, Y.-I.; Lee, J. W.; Kang, J.-W.; Gal, Y.-S.; Kang, S.; Lee, J. Y.; Jung, S.-H.; Kim, H.-S.; Chae, M.-Y.; Jin, S.-H. *Adv. Funct. Mater.* **2009**, *19*, 2205−2212. (d) Liu, X.; Wang, S.; Yao, B.; Zhang, B.; Ho, C.-L.; Wong, W.-Y.; Cheng, Y.; Xie, Z. *Org. Electron.* **2015**, *21*, 1−8. (e) Liu, X.; Yao, B.; Zhang, Z.; Zhao, X.; Zhang, B.; Wong, W.-Y.; Cheng, Y.; Xie, Z. *J. Mater. Chem. C* **2016**, *4*, 5787−5794. (f) Cao, S.; Hao, L.; Lai, W.-Y.; Zhang, H.; Yu, Z.; Zhang, X.; Liu, X.; Huang, W. *J. Mater. Chem. C* **2016**, *4*, 4709−4718. (g) Lin, J.; Chau, N.-Y.; Liao, J.-L.; Wong, W.-Y.; Lu, C.-Y.; Sie, Z.-T.; Chang, C.-H.; Fox, M. A.; Low, P. J.; Lee, G.-H.; Chi, Y. *Organometallics* **2016**, *35*, 1813−1824.

(27) Dolomanov, O. V.; Bourhis, L. J.; Gildea, R. J.; Howard, J. A. K.; Puschmann, H. *J. Appl. Crystallogr.* **2009**, *42*, 339−341.

(28) Sheldrick, G. M. *Acta Crystallogr., Sect. A: Found. Crystallogr.* **2008**, *64*, 112−122.

(29) Sheldrick, G. M. *Acta Crystallogr.* **2015**, *C71*, 3−8.

(30) Perdew, J. P.; Burke, K.; Ernzerhof, M. *Phys. Rev. Lett.* **1996**, *77*, 3865−3868.

(31) (a) Hariharan, P. C.; Pople, J. A. *Theor. Chim. Acta* **1973**, *28*, 213−222. (b) Francl, M. M.; Pietro, W. J.; Hehre, W. J.; Binkley, J. S.; Gordon, M. S.; DeFrees, D. J.; Pople, J. A. *J. Chem. Phys.* **1982**, *77*, 3654−3665.

(32) Dolg, M.; Wedig, U.; Stoll, H.; Preuss, H. *J. Chem. Phys.* **1987**, *86*, 866−872.

(33) (a) Tapia, O. *J. Math. Chem.* **1992**, *10*, 139−181. (b) Tomasi, J.; Persico, M. *Chem. Rev.* **1994**, *94*, 2027−2094.

(34) Frisch, M. J.; Trucks, G. W.; Schlegel, H. B.; Scuseria, G. E.; Robb, M. A.; Cheeseman, J. R.; Scalmani, G.; Barone, V.; Mennucci, B.; Petersson, G. A.; Nakatsuji, H.; Caricato, M.; Li, X.; Hratchian, H.

P.; Izmaylov, A. F.; Bloino, J.; Zheng, G.; Sonnenberg, J. L.; Hada, M.; Ehara, M.; Toyota, K.; Fukuda, R.; Hasegawa, J.; Ishida, M.; Nakajima, T.; Honda, Y.; Kitao, O.; Nakai, H.; Vreven, T.; Montgomery, J. A., Jr.; Peralta, J. E.; Ogliaro, F.; Bearpark, M.; Heyd, J. J.; Brothers, E.; Kudin, K. N.; Staroverov, V. N.; Kobayashi, R.; Normand, J.; Raghavachari, K.; Rendell, A.; Burant, J. C.; Iyengar, S. S.; Tomasi, J.; Cossi, M.; Rega, N.; Millam, J. M.; Klene, M.; Knox, J. E.; Cross, J. B.; Bakken, V.; Adamo, C.; Jaramillo, J.; Gomperts, R.; Stratmann, R. E.; Yazyev, O.; Austin, A. J.; Cammi, R.; Martin, R. L.; Morokuma, K.; Zakrzewski, V. G.; Voth, G. A.; Salvador, P.; Dannenberg, J. J.; Dapprich, S.; Daniels, A. D.; Farkas, Ö.; Foresman, J. B.; Ortiz, J. V.; Cioslowski, J.; Fox, D. J. *Gaussian 09, Revision C.01*; Gaussian, Inc., Wallingford, CT, 2011.